Article

Developmental Cell

The Proprioceptive System Masterminds Spinal Alignment: Insight into the Mechanism of Scoliosis

Graphical Abstract

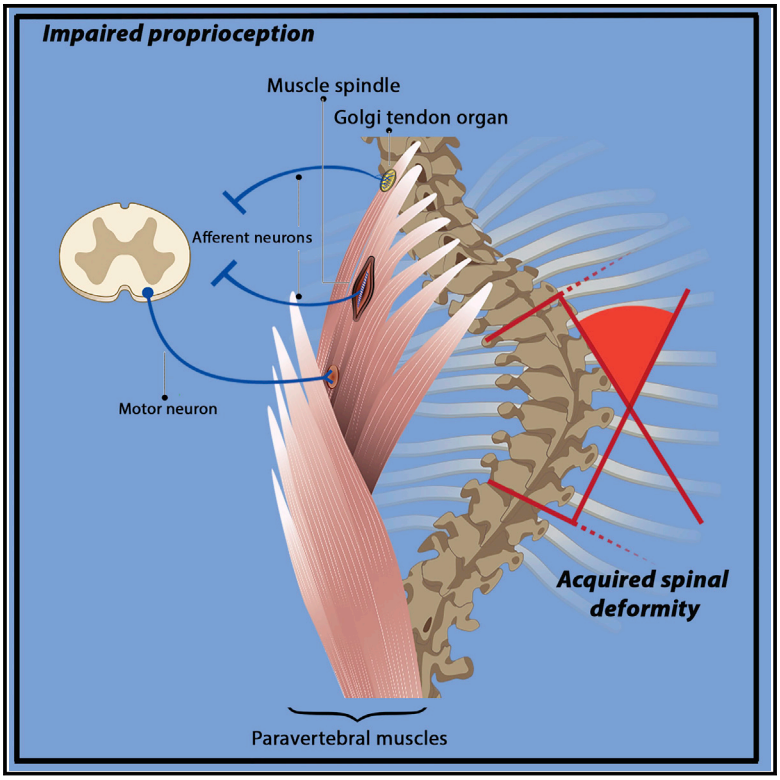

Authors

Ronen Blecher, Sharon Krief, Tal Galili, ..., Gabriel Agar, Yoram Groner, Elazar Zelzer

Correspondence

eli.zelzer@weizmann.ac.il

In Brief

Blecher et al. report that mutant mice lacking functional proprioceptive circuitry develop peripubertal scoliosis not preceded by vertebral dysplasia or muscle asymmetry. Knockout mice lacking one of two proprioceptor types displayed the same, but less severe, phenotype. These findings uncover a central role for proprioception in maintaining spinal alignment.

Highlights

- Knockout mice lacking proprioceptive receptors develop peripubertal scoliosis
- Mice lacking one of the two receptor types develop a less severe spinal phenotype
- Spinal deformity was not preceded by vertebral dysplasia or muscle asymmetry
- The proprioceptive system plays a key role in maintaining spine alignment

Blecher et al., 2017, Developmental Cell *42*, 388–399
August 21, 2017
http://dx.doi.org/10.1016/j.devcel.2017.07.022

CellPress

CellPress

Developmental Cell
Article

The Proprioceptive System Masterminds Spinal Alignment: Insight into the Mechanism of Scoliosis

Ronen Blecher,[1,4] Sharon Krief,[1] Tal Galili,[2] Inbal E. Biton,[3] Tomer Stern,[1] Eran Assaraf,[1,4] Ditsa Levanon,[1] Elena Appel,[1] Yoram Anekstein,[4] Gabriel Agar,[4] Yoram Groner,[1] and Elazar Zelzer[1,5,*]

[1]Department of Molecular Genetics, Weizmann Institute of Science, Rehovot 76100, Israel
[2]Department of Statistics and Operations Research, Tel Aviv University, Tel Aviv 69978, Israel
[3]Department of Veterinary Resources, Weizmann Institute of Science, Rehovot 76100, Israel
[4]Department of Orthopedic Surgery, Assaf HaRofeh Medical Center, Sackler Faculty of Medicine, Tel Aviv University, Zerrifin 70300, Israel
[5]Lead Contact
*Correspondence: eli.zelzer@weizmann.ac.il
http://dx.doi.org/10.1016/j.devcel.2017.07.022

SUMMARY

Maintaining posture requires tight regulation of the position and orientation of numerous spinal components. Yet, surprisingly little is known about this regulatory mechanism, whose failure may result in spinal deformity as in adolescent idiopathic scoliosis. Here, we use genetic mouse models to demonstrate the involvement of proprioception in regulating spine alignment. Null mutants for *Runx3* transcription factor, which lack TrkC neurons connecting between proprioceptive mechanoreceptors and spinal cord, developed peripubertal scoliosis not preceded by vertebral dysplasia or muscle asymmetry. Deletion of *Runx3* in the peripheral nervous system or specifically in peripheral sensory neurons, or of enhancer elements driving *Runx3* expression in proprioceptive neurons, induced a similar phenotype. *Egr3* knockout mice, lacking muscle spindles, but not Golgi tendon organs, displayed a less severe phenotype, suggesting that both receptor types may be required for this regulatory mechanism. These findings uncover a central role for the proprioceptive system in maintaining spinal alignment.

INTRODUCTION

The spine is a highly complex structure, composed of multiple vertebrae linked by dozens of intervertebral discs and synovial joints and fastened by ligaments and tendon insertions. Serving as the central axis of the body, it supports weight and maintains posture while allowing movement. Another key role is to harbor the spinal cord within the spinal canal, where it is protected during movement and growth. Like other skeletal elements, the spine is subjected to immense stresses arising from the organism's weight and from load exerted by the attached muscles. It is widely believed that the spine successfully copes with these stresses due to its unique structure. This structure restricts movement to provide inherent stability and thereby minimizes the need for continuous external stabilization by contraction of adjacent muscles (Rawls and Fisher, 2010).

Scoliosis is a three-dimensional deformity affecting the spinal column and accompanying anatomical structures. The two major forms of scoliosis are the congenital and adolescent subtypes. By far, the most common type of scoliosis is the adolescent subtype, which appears without a known cause and in the absence of skeletal anomalies and is therefore termed adolescent idiopathic scoliosis (AIS). The condition, defined by the Scoliosis Research Society (SRS) as a lateral curvature of the spine of 10° or greater (SRS, 2016a), affects around 3% of school-aged children worldwide. When the deformity progresses, interventions include back bracing, aimed at halting the progression, or surgical correction, which is reserved for severe or rapidly progressing curves (Warner et al., 2013). To date, despite substantial efforts to decipher the pathogenesis of acquired scoliosis, the mechanisms underlying this condition are still elusive (Ouellet and Odent, 2013) Interestingly, the appearance of a curve in patients with morphologically intact spinal elements suggests the involvement of an unknown tissue-non-autonomous mechanism in regulating spinal alignment.

In the musculoskeletal system of numerous species, including mammals, proprioceptive mechanosensors are found in large numbers in most striated muscles (Kokkorogiannis, 2004; Soukup, 1983). In recent years, several molecular pathways that regulate their formation, connectivity, and function have been identified (Arber et al., 2000; Cheret et al., 2013; Friese et al., 2009; Hippenmeyer et al., 2002; Tourtellotte et al., 2001). The two predominant types are the muscle spindle and the Golgi tendon organ (GTO). These types differ in morphology, location, measured input, effect, and other traits (Granit, 1975; Maier, 1997; Moore, 1984). Common to both organs is the ability to sense the biomechanical environment, rapidly initiate a neural response in specialized sensory afferent fibers, and, ultimately, modulate local muscle tension, thus forming the muscle spindle and GTO reflex arches (Proske and Gandevia, 2012). The specialized afferent fibers, termed proprioceptive neurons, transmit mechanical sensations from muscles and tendons via the dorsal root ganglia (DRG) to the spinal cord. These neurons express the neurotropic tyrosine tropomyosin receptor kinase

C (*TrkC*; also known as neurotrophic tyrosine kinase receptor type 3 [*Ntrk3*]) (Marmigere and Ernfors, 2007). Runt related transcription factor 3 (Runx3), a member of the RUNX family of transcription factors, is highly expressed by DRG *TrkC*-positive neurons and is essential for their survival, axonal projection, and connectivity to the spinal cord (Inoue et al., 2003; Levanon et al., 2002). Accordingly, mice lacking *Runx3* develop severe limb ataxia. This *Runx3* knockout (KO) phenotype was recently recapitulated in mice missing the genomic elements regulating *Runx3* expression in DRG TrkC neurons (Appel et al., 2016). In skeletal muscles, differentiation of muscle-spindle-specific fibers is regulated by early growth response 3 (*Egr3*), a member of the zinc-finger family of transcription factors (Oliveira Fernandes and Tourtellotte, 2015; Tourtellotte et al., 2001; Tourtellotte and Milbrandt, 1998).

In this work, we identify a unique mechanism whereby muscle spindles and GTOs act via the proprioceptive stretch reflex circuit to maintain spinal alignment. These findings may advance the understating of the etiology of AIS and provide a mouse model for further studies of this disease.

RESULTS

Runx3 Deficiency Is Associated with Severe Scoliosis

It has previously been speculated that proprioceptive mechanosensors (Barrack et al., 1984; Wyatt et al., 1986; Yamada et al., 1984) and, in particular, muscle spindles (Ford et al., 1988; Low et al., 1983; Yekutiel et al., 1981) might be involved in scoliosis. To test this hypothesis, we studied the skeletons of *Runx3* KO mice, which lack proprioceptive circuitry (Levanon et al., 2002). Spinal alignment of 20 mature *Runx3* KO mice was evaluated at postnatal day 90 (P90) using computed tomography (CT) images and compared with 20 wild-type (WT) littermates. Scoliosis was defined as a lateral curve of the spine greater than 10° in the coronal plane (SRS, 2016a). Results showed that 95% (19/20) of the skeletons of *Runx3* KO mice exhibited scoliosis (Figures 1A–1C). The most observed pattern of deformity was a major thoracic curve accompanied by smaller curves rostrally and caudally. In 84% (16/19) of the deformed spines, the apex of the major curve was right-sided and located between spinal levels T8 and T10. Cobb angle measurement (Cobb, 1948) revealed that curve severity ranged between 12° and 71°. In comparison, only one control mouse (5%) had a curve of 10°, 5 exhibited lesser curves, and the rest had no measurable deformity.

Runx3-Related Scoliosis Is Acquired at the Peripubertal Period

Next, to determine whether the scoliosis observed in *Runx3*-deficient mice was congenital or acquired, we examined spines of KO and WT mice by sequential *in vivo* CT scans at P40, P60, and P90. Of the 10 *Runx3* KO mice examined, only one exhibited spinal deformity in the first postnatal scan (Figures 1D–1F). Strikingly, all other mutant animals acquired a deformity during the following interval (i.e., by P60), which was worsened by P90. Conversely, spines of WT mice remained straight throughout the radiographic follow-up. Deformity appearance was unrelated to sex, as both male and female spines became deformed shortly after reaching pubertal maturity, i.e., between P40 and P60. Similarly, curve severity was unrelated to sex (Figure 1F). Finally, to determine whether the deformity continues to progress at later stages, we scanned mature mice at P150 and P240. Results showed that in the majority of animals spinal deformity continued to progress, but at a slower rate (Figure S1).

Developing Spines of *Runx3* KO Mice Display No Gross Morphological Malformations

Having identified the onset time of *Runx3* KO-associated scoliosis, we proceeded to explore possible non-proprioceptive contributions to the phenotype. To this end, we assessed the involvement of abnormalities in the vertebrae and the intervertebral discs as causative factors in the pathogenesis. Representative vertebrae (T4, T7, T10, T13, and L2) of *Runx3* KO and control littermates were scanned by CT *in vivo* at P14 and P25. Reconstruction followed by registration enabled morphological comparison of the outer surface of matched mutant and control vertebrae. Correction for size discrepancies between smaller mutants and controls was achieved using isotropic scaling (see STAR Methods). In addition, comparison between two control animals was performed to exclude inter-subject variability. Results revealed a marked similarity between the external surfaces of mutant and control vertebrae at both ages and at all examined spinal levels (Figures S2A–S2C).

To quantify these results, we performed morphometric analysis of vertebrae at two time points (P25 and P40) and at various spinal levels using previously reported indices (Masharawi et al., 2008a, 2008b). The ratios between anterior and posterior heights and right and left heights as well as between right and left superior facet angles were measured in mutant and control mice to assess the sagittal, coronal, and axial planes, respectively. Measurements were performed for T4, T7, T10, T13, and L2 in 5 mutant and 5 control animals. Results showed that the mean index ratios at each plane and spinal level in *Runx3* KO mice were similar to those measured in control littermates at both P25 (Figure 2) and P40 (Figure S3).

Next, we compared the structure of D8-D9 intervertebral discs, a level found to be commonly located within the curve apex, between P3 *Runx3* KO mice and WT littermates. Comparisons were made in the coronal and sagittal planes using histological staining (H&E) as well as expression analysis of scleraxis (*Scx*), which was previously shown to be expressed in intervertebral discs and in spinal ligaments and tendons (Sugimoto et al., 2013) Analysis showed that intervertebral disc morphology was similar in *Runx3* KO and control mice (Figures S4D–S4G), with the exception of symmetrically smaller and underdeveloped discs in the KO mice. In addition, comparable *Scx* expression was detected in the anterior longitudinal ligaments of both KO and control mice.

Finally, to assess whether muscle abnormality could explain the deformity observed in KO spines and the right-sided tendency of the curve, we stained sections from P30 *Runx3* KO and littermate control mice for wheat germ agglutinin and myosin. Results showed no differences between right- and left-side muscle fibers in either KO or control mice. Yet *Runx3*-KO muscles displayed significantly reduced mean fiber area compared with control muscles. No differences were observed in myosin expression between strains or between sides (Figure S4).

Together, these results show that although the vertebrae, intervertebral discs, and the attaching muscles of *Runx3* KO

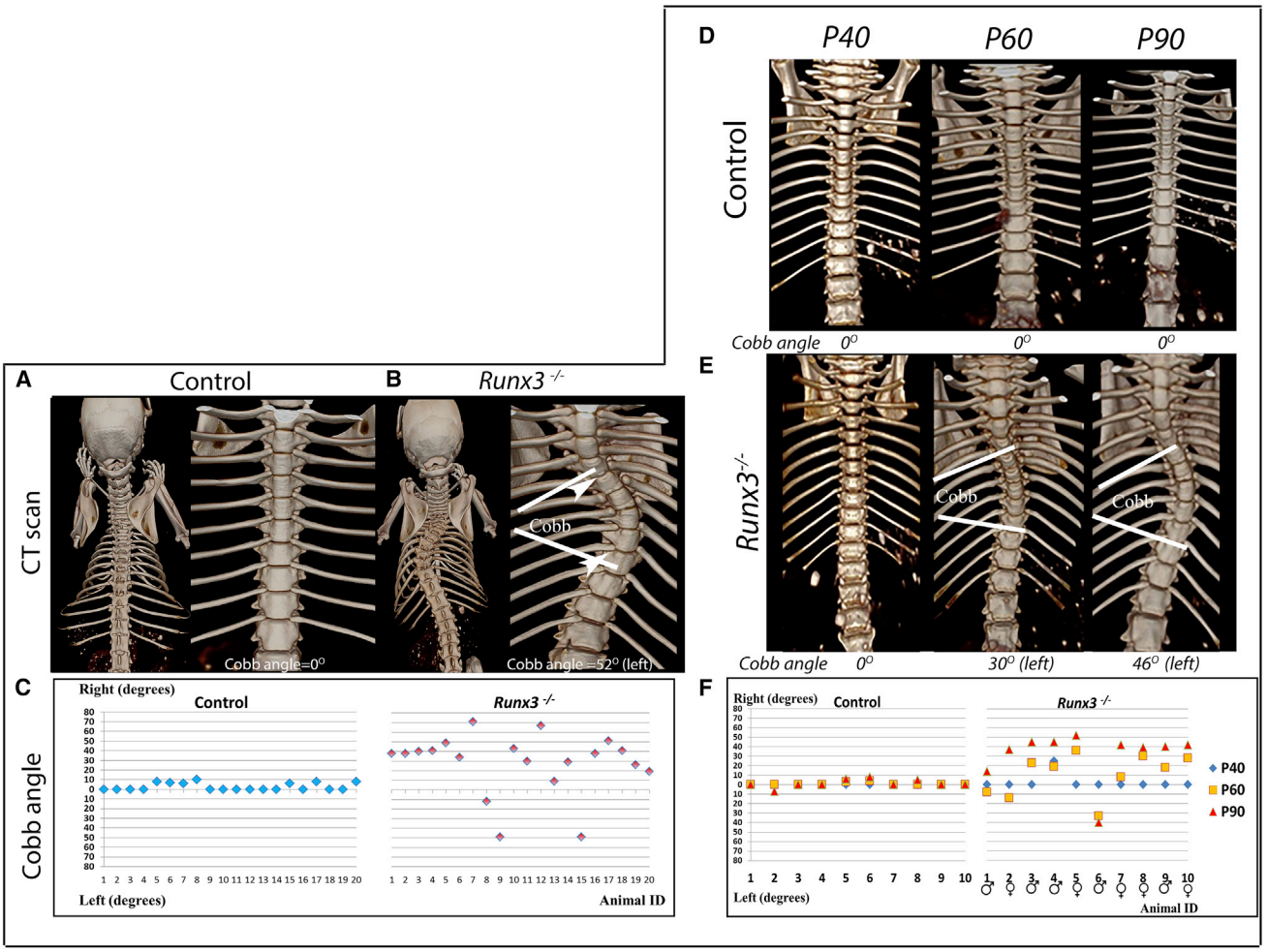

Figure 1. *Runx3*-Deficient Mice Display Scoliosis of Varying Severity

(A and B) CT-scanned skeletal images of representative WT (A) and *Runx3*-KO (B) mice at P90. The two most coronal plane-tilted vertebrae on the caudal and rostral ends of the curve are indicated (B, white arrowheads). The angle between the white lines parallel to the endplate of each of these vertebrae, termed the Cobb angle, indicates the severity of deformity.

(C) Graph showing Cobb angle values for all control (left) and mutant mice (n = 20 in both groups). All but one *Runx3* KO mice (19/20) exhibited scoliosis, mostly of high severity. In contrast, no control animal displayed a curve greater than 10°. Both substantial curves in the *Runx3* KO group and minor curves in the WT had a clear tendency to the right side.

(D and E) Sequential *in vivo* CT scans of spines of WT (D) and *Runx3* KO (E) mice during the postnatal period reveal the temporal dynamics of the onset of *Runx3*-related scoliosis.

(F) Graph showing Cobb angle values for all control (left) and mutant mice during the postnatal period. In the majority of *Runx3* mutants, spinal deformity evolved between P40 and P60. By the following scan (P90) the deformity increased, but to a lesser degree. Both onset time and severity of the deformity were sex-independent. Conversely, spines of control mice remained straight throughout the examined period. See also Figure S1.

mice clearly display developmental delays and reduced size relative to control animals, differences in gross morphology are not likely to play a causative role in the spinal phenotype.

Skeletal Loss of *Runx3* Does Not Affect Spinal Alignment

In addition to its role in the proprioceptive system, *Runx3* is involved in chondrocyte (Stricker et al., 2002; Yoshida et al., 2004) and osteoblast differentiation (Bauer et al., 2015; Lian et al., 2004). We therefore proceeded to examine whether these functions of *Runx3* were associated with the scoliosis phenotype. For this, conditional knockout (cKO) of *Runx3* in osteoblasts or chondrocytes was induced using *Col1a1*- and *Col2a1-Cre* drivers, respectively. Comparison between 3-month-old cKO animals and control littermates showed that ablation of *Runx3* from cells expressing either collagen type I or II did not result in spinal deformity (Figure 3). We therefore concluded that the role of *Runx3* in either osteoblasts or chondroblasts is dispensable. Although *Runx3* was shown to be expressed in the central portion of the vertebral body and in chondrocytes in its periphery (Levanon et al., 2001), it has never been reported to be expressed in spinal tendons or intervertebral discs. Nevertheless, to exclude the possible involvement of *Runx3* expression in these tissues, we eliminated *Runx3* in cells expressing *Scx* (Sugimoto et al., 2013). Comparison of scanned spines of mature (P90) *Scx-Cre-Runx3*

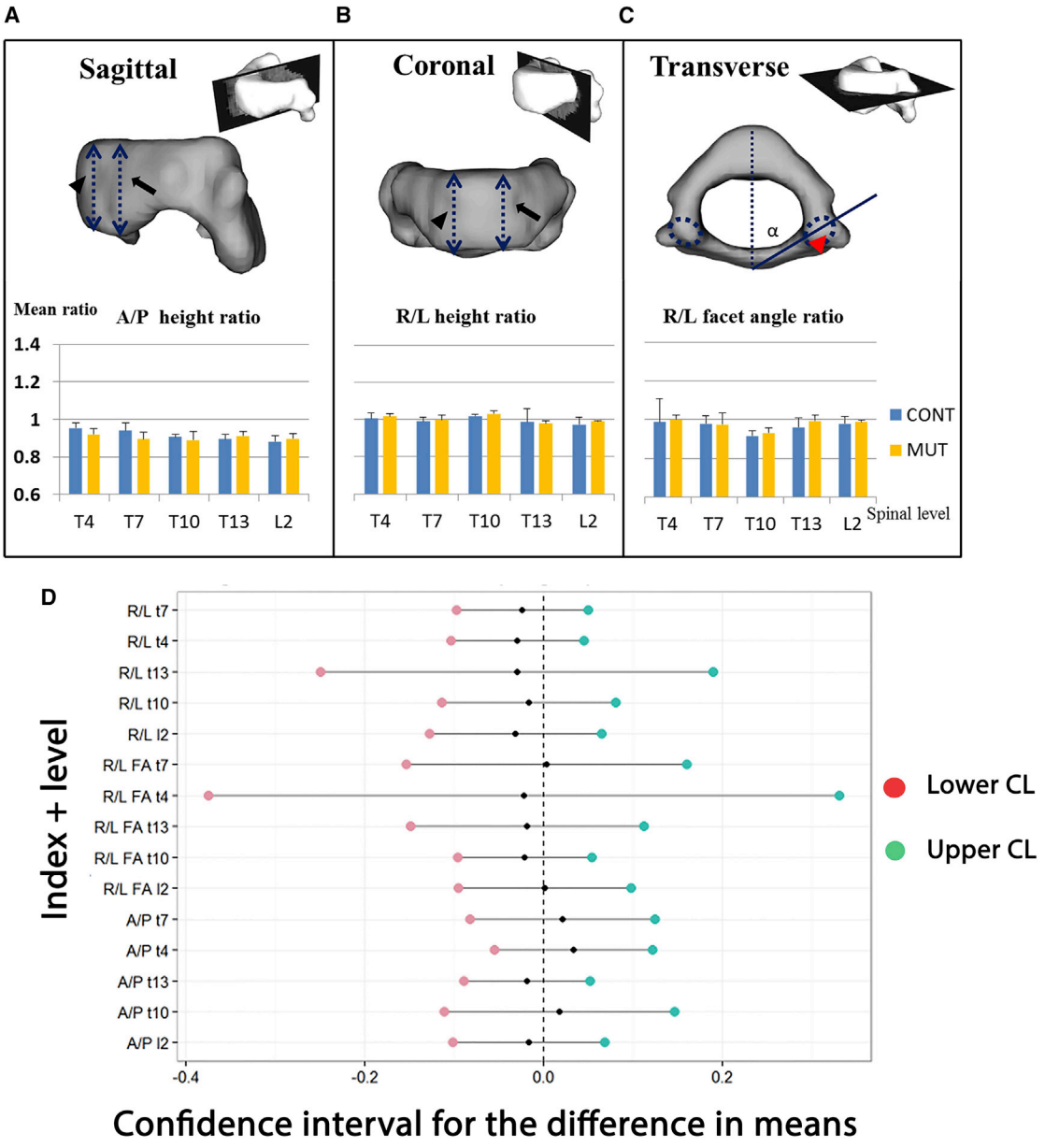

Figure 2. Vertebral Morphometric Analysis at Postnatal Day 25

(A–C) Reconstructed CT-scanned images of vertebrae illustrate the measured features: The ratios between anterior (dashed line indicated by arrowhead) and posterior (dashed line indicated by arrow) heights (A, sagittal plane, A/P ratio), between right (arrowhead) and left (arrow) heights (B, coronal plane, R/L ratio) and between right (dashed circle indicated by arrowhead) and left (dashed circle) superior facet angles (C, transverse plane, R/L facet angle ratio). Graphs below show the morphometric similarity between *Runx3* mutant (MUT) and control (CONT) mice. A/P, anterior/posterior; R/L, right/left.

(D) Graph showing the 95% confidence intervals for differences in mean ratios. Red and green dots indicate upper and lower confidence limits, respectively, and black dots indicate the difference between control and mutant means ratio, which did not exceed the −0.1–0.1 range in all indices and at all levels.

See also Figures S2–S4.

cKO mice and control littermates showed that *Scx*-driven cKO did not result in identifiable scoliosis, indicating that presumable *Runx3* expression in tendons or annulus fibrosus is unrelated to the observed phenotype (Figure S5).

Neuronal Loss of *Runx3* Results in Spinal Malalignment

Having excluded the involvement of skeletal *Runx3* function in promoting scoliosis, we sought to substantiate a direct role of neural expression in the phenotype. For this, we ablated *Runx3* expression conditionally using two neural Cre drivers, namely *Brn3a* and *Wnt1*. *Brn3a-CreER* ^{T2} acts in the peripheral sensory nervous system including the DRG (Dykes et al., 2011; O'Donovan et al., 2014), whereas *Wnt1-Cre* acts in the entire peripheral nervous system (Brault et al., 2001). Expression analysis in the DRG of the two cKO strains revealed complete ablation of *Runx3* expression in *Wnt1-Cre-Runx3* cKO embryos, whereas

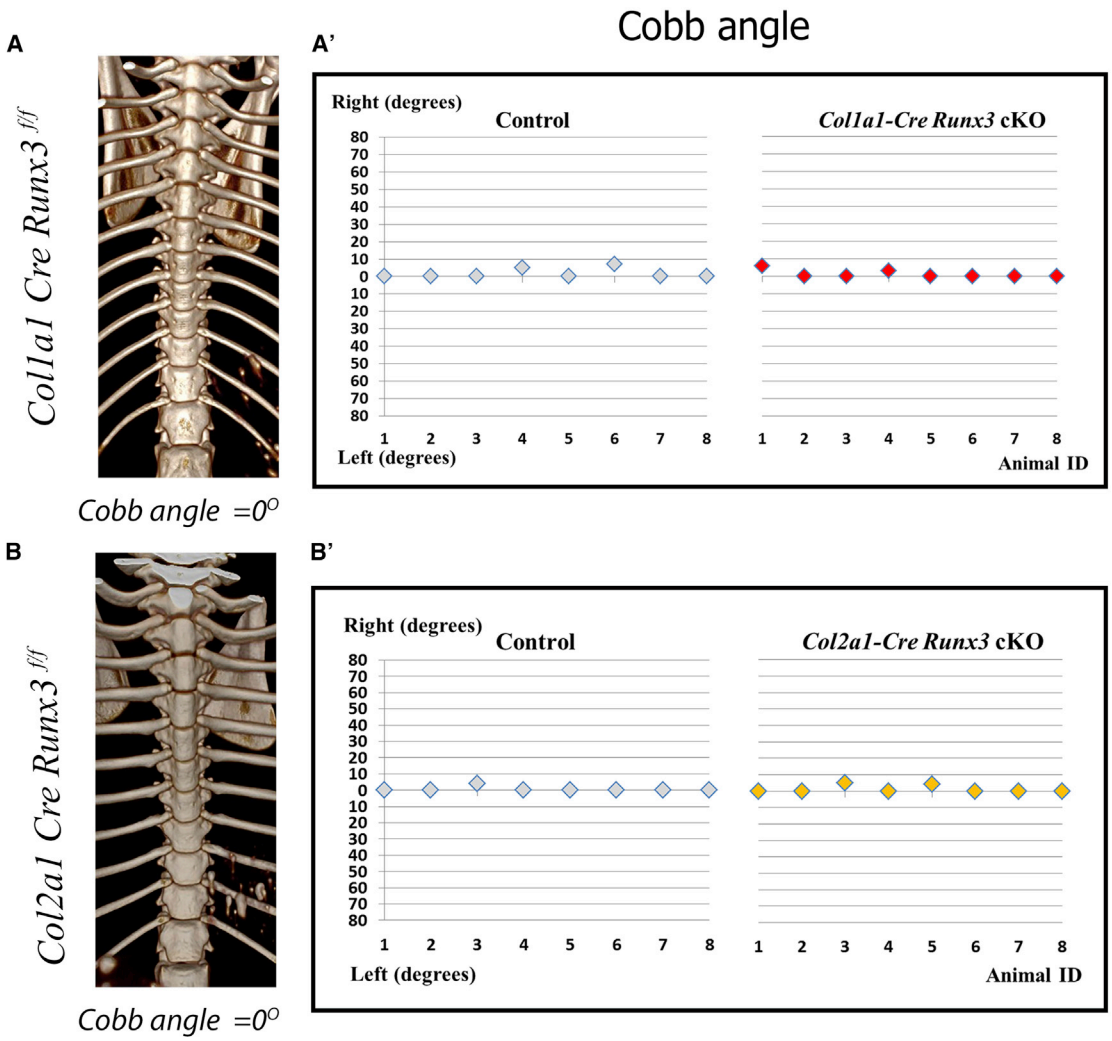

Figure 3. Assessment of Spinal Deformity in *Runx3* Mesenchymal cKO Strains

(A and B) CT-scanned skeletal images of two *Runx3* cKO strains in which *Runx3* was ablated from osteoblasts (*Col1a1-Cre-Runx3*$^{f/f}$; top) or chondrocytes (*Col2a1-Cre-Runx3*$^{f/f}$).

(A′ and B′) Graphs show Cobb angle for the two cKO strains and control mice (P90, n = 8 in all groups), indicating no scoliosis.

See also Figure S5.

Brn3a-CreER^{T2}-driven *Runx3* cKO achieved substantial but incomplete deletion (Figure S6). To verify that *Runx3* ablation disrupts the proprioceptive circuitry, we examined the presence of TrkC neurons in these mice. Co-immunofluorescence for TrkC and RUNX3 in the DRG of *Brn3a-Runx3* cKO mice revealed a reduced number of these proprioceptive neurons, whereas in DRG of *Wnt1-Runx3* cKO mice they were completely absent (Figure S7).

Next, to test the functional effect of neural *Runx3* deletion, we examined newborn mice for posture and gait. As seen in Figure 4, cKO animals displayed a severely impaired gait pattern similar to that of *Runx3*-KO mice, including posterior placement of forelimbs, uncoordinated limb placement, and severe ataxia. To quantify the effect, we functionally assessed gait using the "CatWalk" assay. At the age of 3 months, all cKO animals displayed a decrease in gait regularity. Yet whereas in *Brn3a-Runx3* cKO strain only a small decrease was measured, both *Runx3* KO and *Wnt1-Runx3* cKO mice exhibited a substantial and similar effect (Figure 4).

We then assessed spinal deformity in the two neural cKO strains by *in vivo* CT scans at P90. *Runx3* ablation from neural tissue resulted in scoliosis of varying strain-dependent severity and incidence (Figure 5). *Brn3a-Runx3* cKO mice displayed relatively mild scoliosis with ~40% incidence, compared with a 95% incidence in the *Runx3* KO group ($p < 0.005$). *Wnt1-Runx3* cKO resulted in more pronounced curves than *Brn3a*-driven cKO and ~75% incidence (p-value non-significant relative to *Runx3* KO). As expected, control mice of both cKO strains maintained normal spinal alignment. Interestingly, the direction of the major curve upon neural ablation of *Runx3* was similar to the bend observed in *Runx3* KO mice, namely to the right in the coronal plane.

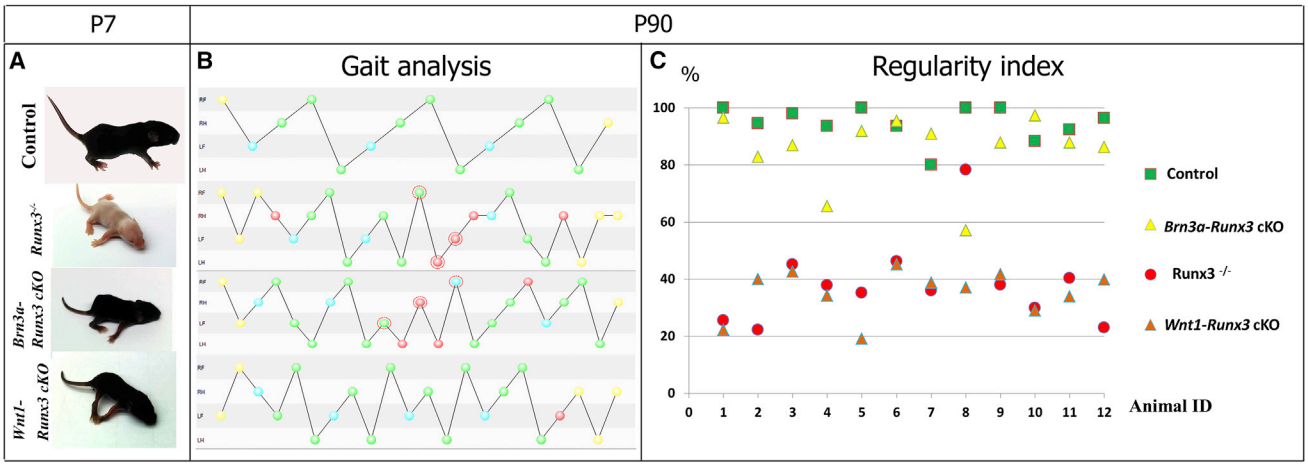

Figure 4. Posture and Gait Analysis of Neuronal *Runx3* cKO Strains

(A) Similarly to *Runx3* KO mice, both cKO strains exhibit impaired posture.

(B and C) CatWalk gait analysis (B) of mature WT and neuronal cKO mice. The regularity index (RI) (C) represents the relative number of sequential paw placements forming a regular pattern (Chen et al., 2014). Control and *Brn3a-Runx3* cKO mice had similar RI values ranging from 0.8 to 1.0, with only a few mutant animals displaying decreased RI. In contrast, *Runx3* KO and *Wnt1-Runx3* cKO mice scored significantly less (0.2–0.5), indicating highly uncoordinated gait. See also Figures S6 and S7.

As already mentioned, it was recently shown that *Runx3* expression by DRG TrkC neurons is mediated by three distinct regulatory elements located upstream of the *Runx3* gene (Appel et al., 2016). To further validate the direct role of neuronal *Runx3* inactivation in the phenotype, we conducted CT scans of mature mice (P90) in which various combinations of the sensory-specific regulatory elements had been deleted. Analysis showed that ablation of all three regulatory elements resulted in spine deformity, although at lower incidence than upon *Runx3* KO (Figure 5). Taken together, these results show that the neural function of *Runx3* plays a key role in the development of *Runx3*-associated scoliosis.

Muscle Spindle Loss Results in Scoliosis

The marked and acquired spinal deformity observed in *Runx3* KO mice supports a key role for the proprioceptive system in maintaining spinal alignment. As already mentioned, proprioception is mediated by two types of peripheral sensors, the muscle spindle and the GTO. To validate their role and determine the relative contributions of the two sensor types to the observed spine deformity, we examined mature mice deficient in *Egr3*, in which muscle spindles fail to survive whereas GTOs are retained (Chen et al., 2002). To assess the impact of muscle spindle dysfunction on gait, we analyzed *Egr3* mutants and control mice using the CatWalk assay. As shown in Figure 6, *Egr3* deficiency resulted in impaired gait, which was less severe relative to *Runx3* mutants. We then evaluated spinal deformity as before. Initial CT scanning at P40 revealed no indication for deformity. However, 3 of 13 *Egr3* mutants developed spinal curves between P40 and P60 and an additional 5 during the subsequent interval (P60–P90; Figure 6). These results reinforce the involvement of muscle proprioceptors in the regulation of spinal alignment. Moreover, the reduced phenotype severity as compared with *Runx3* mutants may indicate that both receptor types are required for maintaining proper alignment of the spine.

DISCUSSION

Deciphering the mechanisms underlying the pathogenesis of AIS has long been a challenge, as the onset of this acquired spinal deformity is not accompanied by other complaints or identifiable anatomical anomalies. Moreover, despite numerous attempts to develop genetic (Adham et al., 2005; Blanco et al., 2001), neuroendocrine (Machida et al., 1995; Thillard, 1959), or surgical perturbation (Pal et al., 1991; Robin, 1996) models for AIS, no model has sufficiently correlated with the unique features of the disease (Ouellet and Odent, 2013). In this study, we present a mouse model in which the spinal deformation process shares several hallmark features with AIS. First, the skeletons of mice with partial or complete proprioception impairment are apparently intact prior to the appearance of scoliosis. Second, the temporal dynamics of the deformative process, which progresses at the highest rate around puberty and more slowly thereafter, and the commonly resultant accentuated right-sided curve of the thoracic spine are both characteristic of AIS.

Over the years, a large body of evidence has accumulated supporting neuromuscular involvement in the etiology of scoliosis. Studies of AIS patients have identified abnormal morphology and function of neuromuscular elements in the CNS (Shi et al., 2013; Wang et al., 2012), the somatosensory (Guo et al., 2006) and vestibular (Shi et al., 2011) systems, and trunk muscles (Acaroglu et al., 2009; McIntire et al., 2007). Further support lies in the clinically well-established association between neural insults, such as stroke (Gillen, 2015) and cerebral palsy (SRS, 2016b), and the development of trunk imbalance and ensuing deformity. Moreover, in several animal models the removal of neural elements such as the spinal cord (Barrios et al., 1987) or nerve roots (Liszka, 1961; MacEwen, 1973; Pincott et al., 1984) resulted in scoliosis, demonstrating the association across species. The indications for impaired proprioception in AIS patients include alterations in postural equilibrium

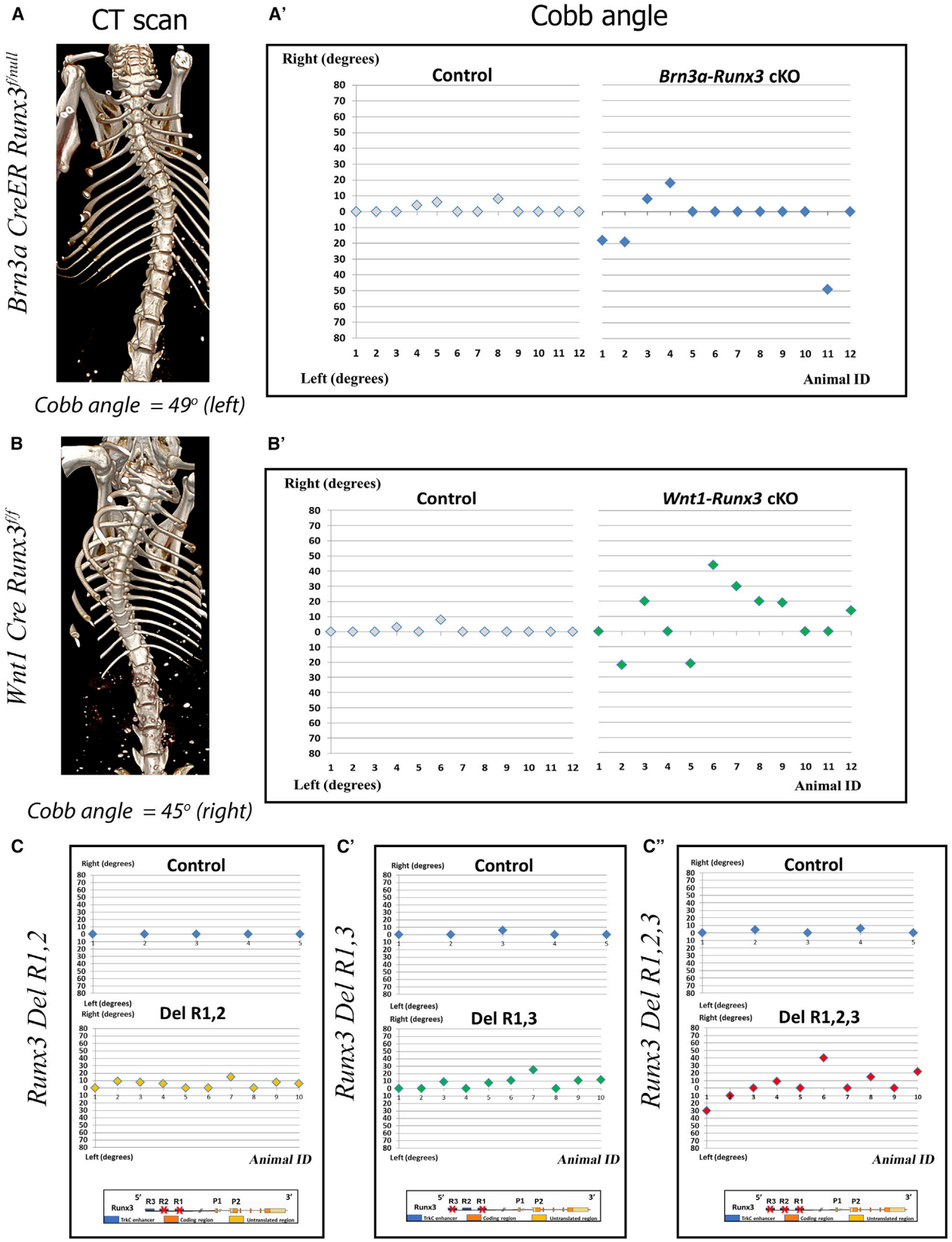

(legend on next page)

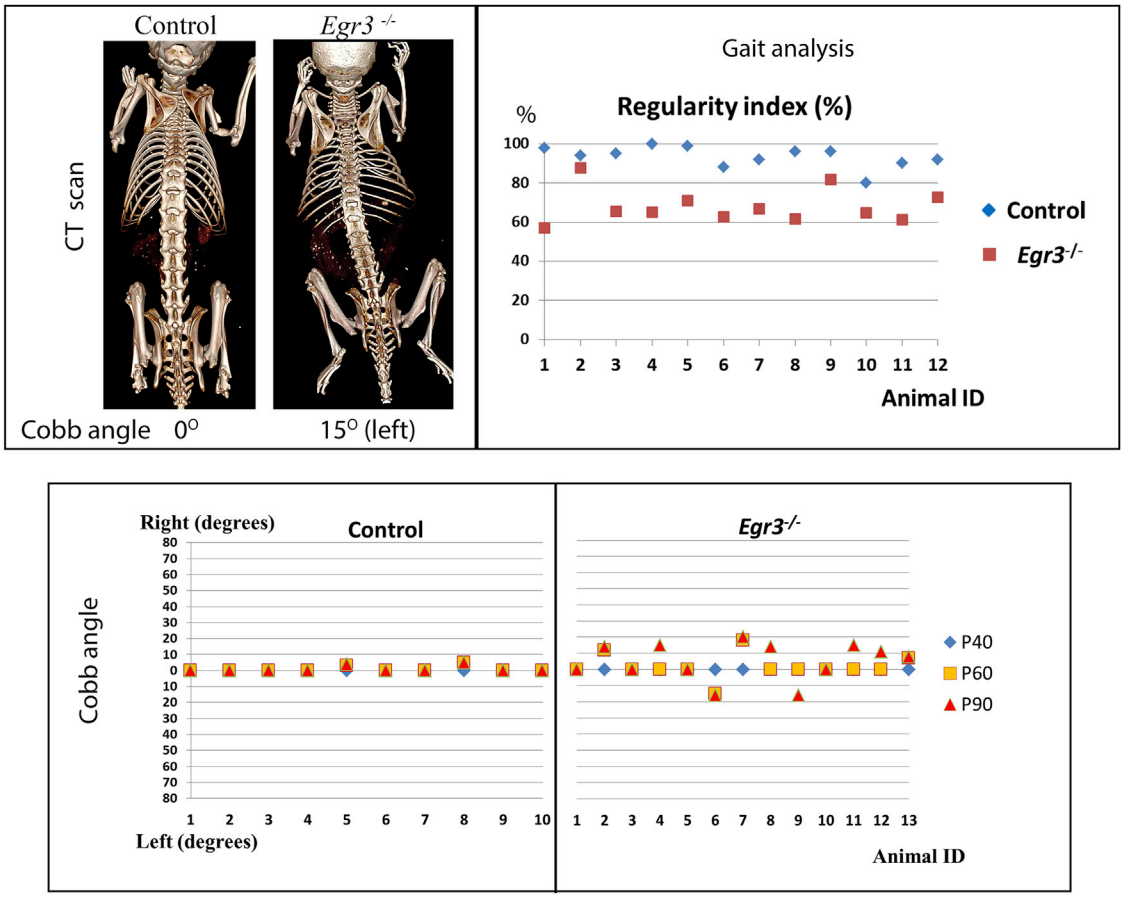

Figure 6. Morphological and Functional Assessment of *Egr3*-Deficient Mice

Top left: *in vivo* CT-scanned skeletons of control (left) and *Egr3*-null mutants. Bottom: Graph summarizing postnatal spinal alignment of WT and *Egr3*-null mice as measured by Cobb angle. Of 13 mutant mice, none exhibited deformity at P40. Yet 3 animals developed deformity between P40 and P60 and 5 more by the last scan (P90), while the already observed deformities did not progress. Overall, curves did not exceed 20°. Top right: graph showing the results of gait analysis. *Egr3* mutants scored RI values between 55% and 90%, representing the relative contribution of muscle spindle dysfunction to the gait impairment observed in *Runx3* mutants.

(Gruber et al., 2011; Lao et al., 2008), gait (Yang et al., 2013), various neural responses (Barrack et al., 1984; Wyatt et al., 1986; Yamada et al., 1984; Yekutiel et al., 1981), and decreased muscle spindle concentration in the paravertebral muscles (Ford et al., 1988).

Interestingly, studies aimed at deciphering the mechanism that controls the stability of a complex structure such as the spine also suggest the involvement of proprioception and, specifically, muscle spindles as a regulatory feedback mechanism (Bergmark, 1989; Reeves et al., 2007). Nevertheless, direct evidence linking impaired proprioception with spinal instability or scoliosis has not been presented. Our work provides a possible missing link between the proprioceptive system and scoliosis by establishing proprioception as a central regulator of spinal alignment. Moreover, our data indicate that both proprioceptor types probably play a role in this process.

Our findings clearly indicate that the proprioceptive system may not only provide an array of dynamic spine stabilizers, but also acts as a gatekeeper that prevents progressive spinal deformation. Recently, we have uncovered another example of proprioceptive regulation of the skeleton. Previously we reported that in fractured humeri of mice, the bone is realigned spontaneously by movement the two fracture fragments, a process we termed natural reduction (Rot et al., 2014). We then showed that muscle spindles and GTOs act as a super-mechanism orchestrating this process (Blecher et al., 2017). The involvement of the proprioceptive system in both maintenance and regeneration of the skeleton increases

Figure 5. Ablation of *Runx3* from the DRG Results in Scoliosis in Mature Mice

In vivo CT-scanned P90 skeletons of sensory-specific (*Brn3a*-driven, top) and pan-peripheral neural (*Wnt1*-driven) *Runx3* cKO mice (A′ and B′) and mice in which various combinations of sensory-specific enhancers had been deleted (C–C″). Graphs show comparison of Cobb angle between the various strains. Scoliosis was more prevalent and more severe in *Wnt1*-driven cKO mice compared with *Brn3a*-driven cKO. Deletion of all three sensory-specific enhancers (C″) resulted in more severe curves compared with deletion of two enhancers (C and C′). See also Figures S6 and S7.

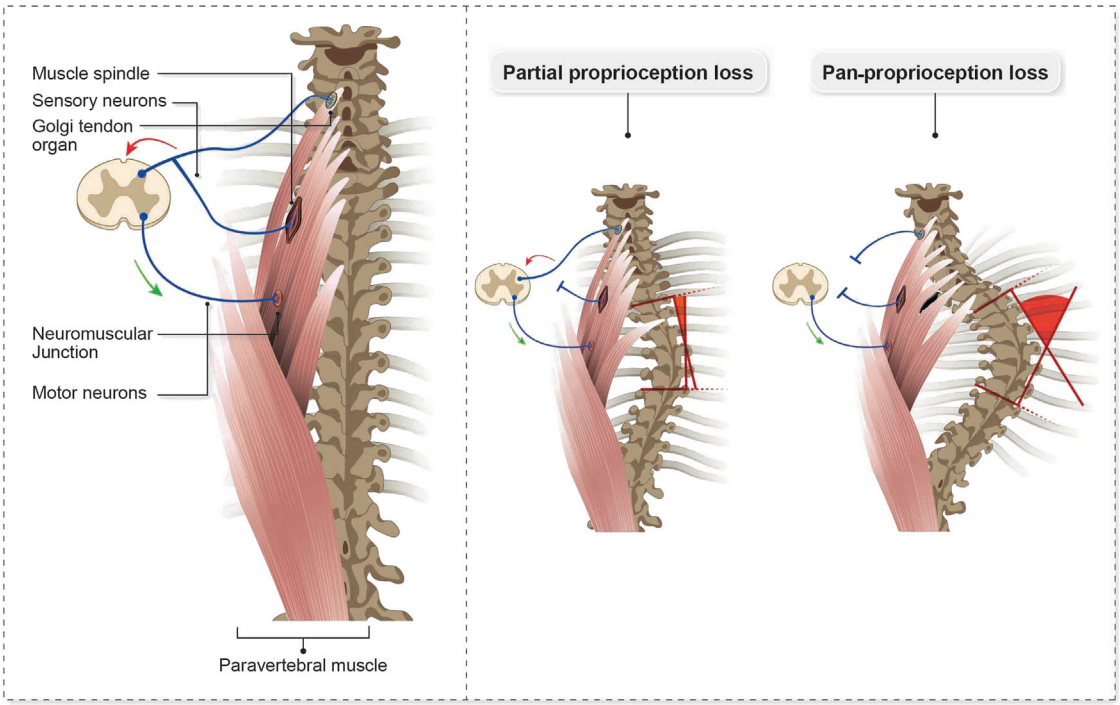

Figure 7. The Proprioceptive System Acts to Maintain Proper Spinal Alignment

In the presence of a functional proprioceptive circuitry, the spine maintains its proper alignment. Removal of muscle spindles alone (partial proprioception loss) results in moderate deformity, whereas the elimination of the entire proprioceptive circuitry (pan-proprioception loss) results in severe deformity.

substantially the scope of known physiological functions of this system.

Our findings raise the question of the cause of the pubertal onset of scoliosis. Spinal deformity was first observed between P40 and P60, a period that coincides with the postnatal maturation of muscle mechanosensors (Maeda et al., 1985; Osawa et al., 1988), a substantial increase in muscle mass (Griffin and Goldspink, 1973), and increased mobility. Peripubertal scoliosis could therefore result from increasing mechanical burden placed on a proprioceptive-deficient spine. Notwithstanding the similarities between our proprioceptive-deficient mouse strains and AIS patients, one major difference is the lack of ataxia in AIS patients. This difference highlights the necessity to dissociate between spinal misalignment and ataxia in the current animal model. Moreover, the co-appearance of these two major phenotypes raises the possibility that in our model, ataxia could contribute to the development of scoliosis. Given the close functional and anatomical interactions between central and peripheral proprioceptive circuits and the limited experimental tools currently available for addressing this issue, the question remains open. Another difference is that while our findings introduce *Runx3* and *Egr3* as primary genes of interest, the etiopathogenesis of AIS has long been considered polygenic in nature (Ikegawa, 2016; Ward et al., 2010). Identification of downstream target genes of *Runx3* and *Egr3* may uncover new molecular players involved in scoliosis.

Another intriguing issue is the phenotypic variability among the analyzed mouse strains. Whereas the less severe phenotype observed in the *Brn3a*-driven cKO strain can be explained by incomplete ablation of *Runx3*, the reduced phenotype in *Wnt1-Runx3* cKO compared with *Runx3* KO mice remains an open question. Although none of *Runx3* ablations in mesenchyme-derived tissues (i.e., *Col1a1-Cre*, *Col1a2-Cre*, and *Scx-Cre*) produced an observed phenotype, it is possible that the effect of concomitant loss of *Runx3* expression in both mesenchyme-derived cells and the neural system increases the severity of the phenotype. In addition, differences in strain background (Levanon et al., 2003) may also contribute to the observed differences in phenotype severity.

The proposed involvement of proprioceptive dysfunction in the etiology of AIS provides a specific target for further exploration. This etiological explanation may promote the search for the genetic background of AIS by focusing attention on genes, loci, and pathways associated with proprioception, complementing the rich literature on various loci associated with susceptibility to AIS (Hayes et al., 2014; Kou et al., 2013; Ogura et al., 2015; Sharma et al., 2015; Takahashi et al., 2011). It may also assist in developing non-genetic evaluation and screening tests based on, for example, the performance of simple proprioceptive-related tasks. Together, the shift in focus in the research of AIS may lead to advancement in diagnostics, in assessing the progression potential and, possibly, to future treatment.

Finally, our model establishes a unique relationship between the maintenance of spinal alignment and the proprioceptive system, which has been known principally for its homeostatic function in regulating muscle tension. According to this model, both sensor types seem to act synergistically (Figure 7). This may hint at additional yet unknown roles of the proprioceptive system as well as

the possible involvement of its malfunction in other musculoskeletal pathologies. Clinically, this notion marks the restoration of neuromuscular balance as a potential target for treatment.

STAR★METHODS

Detailed methods are provided in the online version of this paper and include the following:

- KEY RESOURCES TABLE
- CONTACT FOR REAGENT AND RESOURCE SHARING
- EXPERIMENTAL MODEL AND SUBJECT DETAILS
  - Animals
- METHOD DETAILS
  - Histology and Immunofluorescence
  - *In Vivo* Micro-Computed Tomography
  - Measurements of Spinal Deformity
  - Morphometric Analysis
  - Image Registration
  - Gait Analysis
  - Muscle Fiber Area Analysis
- QUANTIFICATION AND STATISTICAL ANALYSIS
  - Statistical Analysis

SUPPLEMENTAL INFORMATION

Supplemental Information includes seven figures and can be found with this article online at http://dx.doi.org/10.1016/j.devcel.2017.07.022.

AUTHOR CONTRIBUTIONS

R.B. designed and conducted the experiments, analyzed the data, and wrote the paper; S.K. conducted the experiments; T.G. conducted statistical analyses; I.B. conducted imaging experiments; T.S. analyzed the imaging data; E.A. conducted the experiments; D.L. and E.A. conducted the *Runx3* regulatory element deletion experiments; Y.A. and G.A. interpreted the results and provided comparative clinical and anatomical advice; Y.G. supervised the *Runx3* regulatory element deletion experiments and wrote the paper; E.Z. supervised the experiments, analyzed the data, and wrote the paper.

ACKNOWLEDGMENTS

We thank Nitzan Konstantin for expert editorial assistance and all members of the E.Z. laboratory for advice and suggestions. We thank Matthew Warman, Boston Children's Hospital, MA, USA, and Carmen Birchmeier, Max Delbrück Center for Molecular Medicine, Berlin, Germany for advice and encouragement. This study was supported by grants from the European Research Council (ERC) (grant no. 310098), the Jeanne and Joseph Nissim Foundation for Life Sciences Research, the Y. Leon Benoziyo Institute for Molecular Medicine, Beth Rom-Rymer, the Estate of David Levinson, the Jaffe Bernard and Audrey Foundation, Georges Lustgarten Cancer Research Fund, the Estate of Bernard Bishin, and the David and Fela Shapell Family (to E.Z.) and by a grant from the Israel Science Foundation (ISF; to Y.G.). Y.A. is a consultant to the commercial company Premia Spine.

Received: December 8, 2016
Revised: June 10, 2017
Accepted: July 24, 2017
Published: August 21, 2017

REFERENCES

Acaroglu, E., Akel, I., Alanay, A., Yazici, M., and Marcucio, R. (2009). Comparison of the melatonin and calmodulin in paravertebral muscle and platelets of patients with or without adolescent idiopathic scoliosis. Spine *34*, E659–E663.

Adham, I.M., Gille, M., Gamel, A.J., Reis, A., Dressel, R., Steding, G., Brand-Saberi, B., and Engel, W. (2005). The scoliosis (sco) mouse: a new allele of Pax1. Cytogenet. Genome Res. *111*, 16–26.

Appel, E., Weissmann, S., Salzberg, Y., Orlovsky, K., Negreanu, V., Tsoory, M., Raanan, C., Feldmesser, E., Bernstein, Y., Wolstein, O., et al. (2016). An ensemble of regulatory elements controls Runx3 spatiotemporal expression in subsets of dorsal root ganglia proprioceptive neurons. Genes Dev. *30*, 2607–2622.

Arber, S., Ladle, D.R., Lin, J.H., Frank, E., and Jessell, T.M. (2000). ETS gene Er81 controls the formation of functional connections between group Ia sensory afferents and motor neurons. Cell *101*, 485–498.

Barrack, R.L., Whitecloud, T.S., 3rd, Burke, S.W., Cook, S.D., and Harding, A.F. (1984). Proprioception in idiopathic scoliosis. Spine *9*, 681–685.

Barrios, C., Tunon, M.T., De Salis, J.A., Beguiristain, J.L., and Canadell, J. (1987). Scoliosis induced by medullary damage: an experimental study in rabbits. Spine *12*, 433–439.

Bauer, O., Sharir, A., Kimura, A., Hantisteanu, S., Takeda, S., and Groner, Y. (2015). Loss of osteoblast Runx3 produces severe congenital osteopenia. Mol. Cell. Biol. *35*, 1097–1109.

Bergmark, A. (1989). Stability of the lumbar spine. A study in mechanical engineering. Acta Orthop. Scand. Suppl. *230*, 1–54.

Blanco, G., Coulton, G.R., Biggin, A., Grainge, C., Moss, J., Barrett, M., Berquin, A., Marechal, G., Skynner, M., van Mier, P., et al. (2001). The kyphoscoliosis (ky) mouse is deficient in hypertrophic responses and is caused by a mutation in a novel muscle-specific protein. Hum. Mol. Genet. *10*, 9–16.

Blecher, R., Krief, S., Galili, T., Assaraf, E., Stern, T., Anekstein, Y., Agar, G., and Zelzer, E. (2017). The proprioceptive system regulates morphologic restoration of fractured bones. Cell Rep. *20*, Published online August 22, 2017. http://dx.doi.org/10.1016/j.celrep.2017.07.073.

Brault, V., Moore, R., Kutsch, S., Ishibashi, M., Rowitch, D.H., McMahon, A.P., Sommer, L., Boussadia, O., and Kemler, R. (2001). Inactivation of the beta-catenin gene by Wnt1-Cre-mediated deletion results in dramatic brain malformation and failure of craniofacial development. Development *128*, 1253–1264.

Chen, H.H., Tourtellotte, W.G., and Frank, E. (2002). Muscle spindle-derived neurotrophin 3 regulates synaptic connectivity between muscle sensory and motor neurons. J. Neurosci. *22*, 3512–3519.

Chen, Y.J., Cheng, F.C., Sheu, M.L., Su, H.L., Chen, C.J., Sheehan, J., and Pan, H.C. (2014). Detection of subtle neurological alterations by the Catwalk XT gait analysis system. J. Neuroeng. Rehabil. *11*, 62.

Cheret, C., Willem, M., Fricker, F.R., Wende, H., Wulf-Goldenberg, A., Tahirovic, S., Nave, K.A., Saftig, P., Haass, C., Garratt, A.N., et al. (2013). Bace1 and Neuregulin-1 cooperate to control formation and maintenance of muscle spindles. EMBO J. *32*, 2015–2028.

Cobb, J. (1948). Outline for the study of scoliosis. Am. Acad. Orthop. Surg. Instr. Course Lect. *5*, 261–275.

Dacquin, R., Starbuck, M., Schinke, T., and Karsenty, G. (2002). Mouse alpha1(I)-collagen promoter is the best known promoter to drive efficient Cre recombinase expression in osteoblast. Dev. Dyn. *224*, 245–251.

Danielian, P.S., Muccino, D., Rowitch, D.H., Michael, S.K., and McMahon, A.P. (1998). Modification of gene activity in mouse embryos *in utero* by a tamoxifen-inducible form of Cre recombinase. Curr. Biol. *8*, 1323–1326.

Dykes, I.M., Tempest, L., Lee, S.I., and Turner, E.E. (2011). Brn3a and Islet1 act epistatically to regulate the gene expression program of sensory differentiation. J. Neurosci. *31*, 9789–9799.

Ford, D.M., Bagnall, K.M., Clements, C.A., and McFadden, K.D. (1988). Muscle spindles in the paraspinal musculature of patients with adolescent idiopathic scoliosis. Spine *13*, 461–465.

Friese, A., Kaltschmidt, J.A., Ladle, D.R., Sigrist, M., Jessell, T.M., and Arber, S. (2009). Gamma and alpha motor neurons distinguished by expression of transcription factor Err3. Proc. Natl. Acad. Sci. USA *106*, 13588–13593.

Gillen, G. (2015). Trunk control: supporting functional independence. In Stroke Rehabilitation: A Function-Based Approach, G. Gillen, ed. (Elsevier), pp. 360–393.

Granit, R. (1975). The functional role of the muscle spindles—facts and hypotheses. Brain *98*, 531–556.

Griffin, G.E., and Goldspink, G. (1973). The increase in skeletal muscle mass in male and female mice. Anat. Rec. *177*, 465–469.

Gruber, A.H., Busa, M.A., Gorton Iii, G.E., Van Emmerik, R.E., Masso, P.D., and Hamill, J. (2011). Time-to-contact and multiscale entropy identify differences in postural control in adolescent idiopathic scoliosis. Gait Posture *34*, 13–18.

Guo, X., Chau, W.W., Hui-Chan, C.W., Cheung, C.S., Tsang, W.W., and Cheng, J.C. (2006). Balance control in adolescents with idiopathic scoliosis and disturbed somatosensory function. Spine *31*, E437–E440.

Hayes, M., Gao, X., Yu, L.X., Paria, N., Henkelman, R.M., Wise, C.A., and Ciruna, B. (2014). ptk7 mutant zebrafish models of congenital and idiopathic scoliosis implicate dysregulated Wnt signalling in disease. Nat. Commun. *5*, 4777.

Hippenmeyer, S., Shneider, N.A., Birchmeier, C., Burden, S.J., Jessell, T.M., and Arber, S. (2002). A role for neuregulin1 signaling in muscle spindle differentiation. Neuron *36*, 1035–1049.

Ikegawa, S. (2016). Genomic study of adolescent idiopathic scoliosis in Japan. Scoliosis Spinal Disord. *11*, 5.

Inoue, K., Ozaki, S., Ito, K., Iseda, T., Kawaguchi, S., Ogawa, M., Bae, S.C., Yamashita, N., Itohara, S., Kudo, N., et al. (2003). Runx3 is essential for the target-specific axon pathfinding of trkc-expressing dorsal root ganglion neurons. Blood Cells Mol. Dis. *30*, 157–160.

Kokkorogiannis, T. (2004). Somatic and intramuscular distribution of muscle spindles and their relation to muscular angiotypes. J. Theor. Biol. *229*, 263–280.

Kou, I., Takahashi, Y., Johnson, T.A., Takahashi, A., Guo, L., Dai, J., Qiu, X., Sharma, S., Takimoto, A., Ogura, Y., et al. (2013). Genetic variants in GPR126 are associated with adolescent idiopathic scoliosis. Nat. Genet. *45*, 676–679.

Lao, M.L., Chow, D.H., Guo, X., Cheng, J.C., and Holmes, A.D. (2008). Impaired dynamic balance control in adolescents with idiopathic scoliosis and abnormal somatosensory evoked potentials. J. Pediatr. Orthop. *28*, 846–849.

Levanon, D., Brenner, O., Negreanu, V., Bettoun, D., Woolf, E., Eilam, R., Lotem, J., Gat, U., Otto, F., Speck, N., et al. (2001). Spatial and temporal expression pattern of Runx3 (Aml2) and Runx1 (Aml1) indicates non-redundant functions during mouse embryogenesis. Mech. Dev. *109*, 413–417.

Levanon, D., Bettoun, D., Harris-Cerruti, C., Woolf, E., Negreanu, V., Eilam, R., Bernstein, Y., Goldenberg, D., Xiao, C., Fliegauf, M., et al. (2002). The Runx3 transcription factor regulates development and survival of TrkC dorsal root ganglia neurons. Embo J. *21*, 3454–3463.

Levanon, D., Brenner, O., Otto, F., and Groner, Y. (2003). Runx3 knockouts and stomach cancer. EMBO Rep. *4*, 560–564.

Levanon, D., Bernstein, Y., Negreanu, V., Bone, K.R., Pozner, A., Eilam, R., Lotem, J., Brenner, O., and Groner, Y. (2011). Absence of Runx3 expression in normal gastrointestinal epithelium calls into question its tumour suppressor function. EMBO Mol. Med. *3*, 593–604.

Levanon, D., and Groner, Y. (2009). Runx3-deficient mouse strains circa 2008: resemblance and dissimilarity. Blood Cells Mol. Dis. *43*, 1–5.

Lian, J.B., Javed, A., Zaidi, S.K., Lengner, C., Montecino, M., van Wijnen, A.J., Stein, J.L., and Stein, G.S. (2004). Regulatory controls for osteoblast growth and differentiation: role of Runx/Cbfa/AML factors. Crit. Rev. Eukaryot. Gene Expr. *14*, 1–41.

Liszka, O. (1961). Spinal cord mechanisms leading to scoliosis in animal experiments. Acta Med. Pol. *2*, 45–63.

Low, W.D., Chew, E.C., Kung, L.S., Hsu, L.C., and Leong, J.C. (1983). Ultrastructures of nerve fibers and muscle spindles in adolescent idiopathic scoliosis. Clin. Orthop. Relat. Res. 217–221.

MacEwen, G.D. (1973). Experimental scoliosis. Clin. Orthop. Relat. Res. 69–74.

Machida, M., Dubousset, J., Imamura, Y., Iwaya, T., Yamada, T., and Kimura, J. (1995). Role of melatonin deficiency in the development of scoliosis in pinealectomised chickens. J. Bone Joint Surg. Br. *77*, 134–138.

Maeda, N., Osawa, K., Masuda, T., Hakeda, Y., and Kumegawa, M. (1985). Postnatal development of the annulospiral endings of Ia fibers in muscle spindles of mice. Acta Anat. (Basel) *124*, 42–46.

Maier, A. (1997). Development and regeneration of muscle spindles in mammals and birds. Int. J. Dev. Biol. *41*, 1–17.

Marmigere, F., and Ernfors, P. (2007). Specification and connectivity of neuronal subtypes in the sensory lineage. Nat. Rev. Neurosci. *8*, 114–127.

Masharawi, Y., Salame, K., Mirovsky, Y., Peleg, S., Dar, G., Steinberg, N., and Hershkovitz, I. (2008a). Vertebral body shape variation in the thoracic and lumbar spine: characterization of its asymmetry and wedging. Clin. Anat. *21*, 46–54.

Masharawi, Y.M., Peleg, S., Albert, H.B., Dar, G., Steingberg, N., Medlej, B., Abbas, J., Salame, K., Mirovski, Y., Peled, N., et al. (2008b). Facet asymmetry in normal vertebral growth: characterization and etiologic theory of scoliosis. Spine *33*, 898–902.

McIntire, K.L., Asher, M.A., Burton, D.C., and Liu, W. (2007). Trunk rotational strength asymmetry in adolescents with idiopathic scoliosis: an observational study. Scoliosis *2*, 9.

Moore, J.C. (1984). The Golgi tendon organ: a review and update. Am. J. Occup. Ther. *38*, 227–236.

O'Donovan, K.J., Ma, K., Guo, H., Wang, C., Sun, F., Han, S.B., Kim, H., Wong, J.K., Charron, J., Zou, H., et al. (2014). B-RAF kinase drives developmental axon growth and promotes axon regeneration in the injured mature CNS. J. Exp. Med. *211*, 801–814.

Ogura, Y., Kou, I., Miura, S., Takahashi, A., Xu, L., Takeda, K., Takahashi, Y., Kono, K., Kawakami, N., Uno, K., et al. (2015). A functional SNP in BNC2 is associated with adolescent idiopathic scoliosis. Am. J. Hum. Genet. *97*, 337–342.

Oliveira Fernandes, M., and Tourtellotte, W.G. (2015). Egr3-dependent muscle spindle stretch receptor intrafusal muscle fiber differentiation and fusimotor innervation homeostasis. J. Neurosci. *35*, 5566–5578.

Osawa, K., Maeda, N., Sato, M., Kawasaki, T., Masuda, T., Yamamoto, Y., Hakeda, Y., Ukai, M., Watanabe, Y., Suwa, T., et al. (1988). Postnatal development of the annulospiral endings of Ia fibers in muscle spindles of the mouse temporal muscle. Anat. Anz. *167*, 253–257.

Ouellet, J., and Odent, T. (2013). Animal models for scoliosis research: state of the art, current concepts and future perspective applications. Eur. Spine J. *22* (*Suppl 2*), S81–S95.

Ovchinnikov, D.A., Deng, J.M., Ogunrinu, G., and Behringer, R.R. (2000). Col2a1-directed expression of Cre recombinase in differentiating chondrocytes in transgenic mice. Genesis *26*, 145–146.

Pal, G.P., Bhatt, R.H., and Patel, V.S. (1991). Mechanism of production of experimental scoliosis in rabbits. Spine *16*, 137–142.

Pincott, J.R., Davies, J.S., and Taffs, L.F. (1984). Scoliosis caused by section of dorsal spinal nerve roots. J. Bone Joint Surg. Br. *66*, 27–29.

Proske, U., and Gandevia, S.C. (2012). The proprioceptive senses: their roles in signaling body shape, body position and movement, and muscle force. Physiol. Rev. *92*, 1651–1697.

Pryce, B.A., Brent, A.E., Murchison, N.D., Tabin, C.J., and Schweitzer, R. (2007). Generation of transgenic tendon reporters, ScxGFP and ScxAP, using regulatory elements of the scleraxis gene. Dev. Dyn. *236*, 1677–1682.

R Development Core Team. (2016). R: A Language and Environment for Statistical Computing (R Foundation for Statistical Computing).

Rawls, A., and Fisher, R.E. (2010). Development and functional anatomy of the spine. In The Genetics and Development of Scoliosis, K. Kusumi and S.L. Dunwoodie, eds. (Springer), pp. 21–46.

Reeves, N.P., Narendra, K.S., and Cholewicki, J. (2007). Spine stability: the six blind men and the elephant. Clin. Biomech. (Bristol, Avon) *22*, 266–274.

Robin, G.C. (1996). Scoliosis induced by rib resection in chickens. J. Spinal Disord. *9*, 351.

Rot, C., Stern, T., Blecher, R., Friesem, B., and Zelzer, E. (2014). A mechanical Jack-like Mechanism drives spontaneous fracture healing in neonatal mice. Dev. Cell *31*, 159–170.

Rueckert, D., Sonoda, L.I., Hayes, C., Hill, D.L., Leach, M.O., and Hawkes, D.J. (1999). Nonrigid registration using free-form deformations: application to breast MR images. IEEE Trans. Med. Imaging *18*, 712–721.

Schnabel, J.A., Rueckert, D., Quist, M., Blackall, J.M., Castellano-Smith, A.D., Hartkens, T., Penny, G.P., Hall, W.A., Liu, H., Truwit, C.L., et al. (2001). A generic framework for non-rigid registration based on non-uniform multi-level free-form deformations. In Medical Image Computing and Computer-Assisted Intervention—MICCAI 2001, M.A. Viergever and W.J. Niessen, eds. (Springer), pp. 573–581.

Sharma, S., Londono, D., Eckalbar, W.L., Gao, X., Zhang, D., Mauldin, K., Kou, I., Takahashi, A., Matsumoto, M., Kamiya, N., et al. (2015). A PAX1 enhancer locus is associated with susceptibility to idiopathic scoliosis in females. Nat. Commun. *6*, 6452.

Shi, L., Wang, D., Chu, W.C., Burwell, G.R., Wong, T.T., Heng, P.A., and Cheng, J.C. (2011). Automatic MRI segmentation and morphoanatomy analysis of the vestibular system in adolescent idiopathic scoliosis. Neuroimage *54* (*Suppl 1*), S180–S188.

Shi, L., Wang, D., Hui, S.C., Tong, M.C., Cheng, J.C., and Chu, W.C. (2013). Volumetric changes in cerebellar regions in adolescent idiopathic scoliosis compared with healthy controls. Spine J. *13*, 1904–1911.

Soukup, T. (1983). The number, distribution and size of Golgi tendon organs in developing and adult rat muscles. Physiol. Bohemoslov. *32*, 211–224.

SRS. (2016a). Adolescent Idiopathic Scoliosis (Scoliosis Research Society).

SRS. (2016b). Neuromuscular Scoliosis (Scoliosis Research Society).

Stricker, S., Fundele, R., Vortkamp, A., and Mundlos, S. (2002). Role of Runx genes in chondrocyte differentiation. Dev. Biol. *245*, 95–108.

Studholme, C., Hill, D.L.G., and Hawkes, D.J. (1999). An overlap invariant entropy measure of 3D medical image alignment. Pattern Recogn. *32*, 71–86.

Sugimoto, Y., Takimoto, A., Hiraki, Y., and Shukunami, C. (2013). Generation and characterization of ScxCre transgenic mice. Genesis *51*, 275–283.

Takahashi, Y., Kou, I., Takahashi, A., Johnson, T.A., Kono, K., Kawakami, N., Uno, K., Ito, M., Minami, S., Yanagida, H., et al. (2011). A genome-wide association study identifies common variants near LBX1 associated with adolescent idiopathic scoliosis. Nat. Genet. *43*, 1237–1240.

Thillard, M.J. (1959). Vertebral column deformities following epiphysectomy in the chick. C. R. Hebd. Seances Acad. Sci. *248*, 1238–1240.

Tourtellotte, W.G., Keller-Peck, C., Milbrandt, J., and Kucera, J. (2001). The transcription factor Egr3 modulates sensory axon-myotube interactions during muscle spindle morphogenesis. Dev. Biol. *232*, 388–399.

Tourtellotte, W.G., and Milbrandt, J. (1998). Sensory ataxia and muscle spindle agenesis in mice lacking the transcription factor Egr3. Nat. Genet. *20*, 87–91.

Wang, D., Shi, L., Chu, W.C., Burwell, R.G., Cheng, J.C., and Ahuja, A.T. (2012). Abnormal cerebral cortical thinning pattern in adolescent girls with idiopathic scoliosis. Neuroimage *59*, 935–942.

Ward, K., Ogilvie, J., Argyle, V., Nelson, L., Meade, M., Braun, J., and Chettier, R. (2010). Polygenic inheritance of adolescent idiopathic scoliosis: a study of extended families in Utah. Am. J. Med. Genet. *152A*, 1178–1188.

Wickham, H. (2009). ggplot2: Elegant Graphics for Data Analysis (Springer-Verlag).

Warner, W.C., Sawyer, J.R., and Kelly, D.M. (2013). Scoliosis and kyphosis. In Campbell's Operative Orthopaedics, J.H. Beaty and S. Terry Canale, eds. (Elsevier), pp. 1703–1896.

Wyatt, M.P., Barrack, R.L., Mubarak, S.J., Whitecloud, T.S., and Burke, S.W. (1986). Vibratory response in idiopathic scoliosis. J. Bone Joint Surg. Br. *68*, 714–718.

Yamada, K., Yamamoto, H., Nakagawa, Y., Tezuka, A., Tamura, T., and Kawata, S. (1984). Etiology of idiopathic scoliosis. Clin. Orthop. Relat. Res. *Apr*, 50–57.

Yang, J.H., Suh, S.W., Sung, P.S., and Park, W.H. (2013). Asymmetrical gait in adolescents with idiopathic scoliosis. Eur. Spine J. *22*, 2407–2413.

Yekutiel, M., Robin, G.C., and Yarom, R. (1981). Proprioceptive function in children with adolescent idiopathic scoliosis. Spine *6*, 560–566.

Yoshida, C.A., Yamamoto, H., Fujita, T., Furuichi, T., Ito, K., Inoue, K., Yamana, K., Zanma, A., Takada, K., Ito, Y., et al. (2004). Runx2 and Runx3 are essential for chondrocyte maturation, and Runx2 regulates limb growth through induction of Indian hedgehog. Genes Dev. *18*, 952–963.

STAR★METHODS

KEY RESOURCES TABLE

REAGENT or RESOURCE	SOURCE	IDENTIFIER
Antibodies		
Rabbit anti-RUNX3	Levanon et al., 2011	N/A
Wheat Germ Agglutinin, Alexa Fluor™ 488 Conjugate	Invitrogen	Cat#W11261
MF 20 antibody	Developmental Studies Hybridoma Bank (DSHB)	DSHB Hybridoma Product MF 20; RRID: AB_2147781
Anti-RFP antibody (Biotin)	Abcam	Cat#ab34771; RRID: AB_777699
Chemicals, Peptides, and Recombinant Proteins		
Tamoxifen	Sigma-Aldrich, Israel	10540-29-1
Tween 20	Sigma-Aldrich, Israel	9005-64-5
Goat serum	Sigma-Aldrich, Israel	Cat#G9023
Bovine serum albumin (BSA)	Sigma-Aldrich, Israel	9048-46-8
Phosphate-buffered saline (PBS)	Gibco by Life Technololgies, UK	Cat#14200-067
DAPI (4',6-diamidino-2-phenylindole)	Sigma-Aldrich, Israel	28718-90-3
Domitor (medetomidine)	Orion, Finland	N/A
Clorketam (ketamine)	Vetoquinol, France	N/A
Antisedan (atipamezole)	Orion, Finland	N/A
Critical Commercial Assays		
CatWalk XT 10.6	Noldus Information Technology	N/A
Experimental Models: Organisms/Strains		
Mouse: ICR	Envigo , Israel	Hsd:ICR (CD-1)
Mouse: C57BL/6	Envigo , Israel	C57BL/6JOlaHsd
Mouse: *Rosa26-tdTomato*	The Jackson Laboratory	JAX: 007905
Software and Algorithms		
ImageJ	ImageJ	http://imagej.net
Amira version 5.2.2	Visage Imaging	http://www.visageimaging.com/
Image Registration Toolkit (IRTK)	Rueckert et al., 1999; Schnabel et al., 2001; Studholme et al., 1999	https://github.com/BioMedIA/IRTK
R	R Development Core Team, 2016	https://www.r-project.org/
ggplot2	Wickham, 2009	http://ggplot2.org/

CONTACT FOR REAGENT AND RESOURCE SHARING

Further information and requests for resources and reagents should be directed to and will be fulfilled by the Lead Contact, Elazar Zelzer (eli.zelzer@weizmann.ac.il).

EXPERIMENTAL MODEL AND SUBJECT DETAILS

Animals

All experiments involving mice were approved by the Institutional Animal Care and Use Committee (IACUC) of the Weizmann Institute. The generation of *Runx3*-null (KO; ICR background) (Levanon et al., 2002), *Egr3*-null (KO; C57BL/6 background) (Tourtellotte and Milbrandt, 1998), loxP-flanked (floxed) *Runx3* (*Runx3*$^{loxP/loxP}$) (Levanon and Groner, 2009), *Col1α1-Cre* (Dacquin et al., 2002), *Col2α1-Cre* (Ovchinnikov et al., 2000), *Brn3a-CreER*^{T2} (O'Donovan et al., 2014), *Wnt1-Cre* (Danielian et al., 1998) and *ScxGFP* (Pryce et al., 2007) mice have been described previously. *Col1a1-Runx3*, *Col2a1-Runx3*, *Brn3a-CreER*^{T2}*-Runx3* and *Wnt1-Runx3* cKO mutants were generated by using males bearing the relevant Cre and a single *Runx3*-floxed allele (*loxP*/+). Each male was then crossed with a female homozygous for the *Runx3 loxP* allele to produce cKO mutants. In each strain, animals lacking Cre (*loxP*/*loxP* or *loxP*/+) served as control littermates. *Rosa26-tdTomato* mice were purchased from The Jackson Laboratory (007905). In all timed pregnancies, plug date was defined as E0.5. With the exception of *Runx3* (ICR) and *Egr3* (Bl/6) null mutants, all other strains were of mixed background.

METHOD DETAILS

Histology and Immunofluorescence

For expression analysis of *Brn3a* and *Wnt1* in the DRG, we performed cryosection immunofluorescence of E12.5 embryos. In the *Brn3a* cKO strain, a single dose of 120 μl tamoxifen (concentration, 20 mg/ml in corn oil) was administered to pregnant females by oral gavage at E10.5. For cryosection immunofluorescence, freshly dissected spines were fixed for 3 hours in 4% PFA, transferred to 30% sucrose overnight, embedded in OCT (Tissue-Tek) and sectioned at a thickness of 10 μm. Cryosections were dried and permeabilized with PBT (0.1% Tween 20/PBS). To block non-specific binding of immunoglobulin, sections were incubated with 7% goat serum 1% BSA in PBT. Cryosections were incubated overnight at 4°C with primary antibody Rabbit anti-RUNX3 (Levanon et al., 2011) (diluted 1:1000). Then, sections were washed in PBT and incubated with secondary antibody Alexa Fluor 488 (Molecular Probes; diluted 1:100). Samples were then washed and stained with DAPI (4',6-diamidino-2-phenylindole, Sigma) for 10 minutes. Finally, sections were mounted on glass slides and examined with laser-scanning confocal microscope LSM 780 (Carl Zeiss).

Muscle staining was performed on cryosections from P30 mice. Antibodies used included WGA (Wheat Germ Agglutinin, Alexa Fluor 488 Conjugate, Invitrogen) and MF 20 antibody (deposited to the Developmental Studies Hybridoma Bank (DSHB), University of Iowa, by Fischman, D.A. (DSHB Hybridoma Product MF 20)).

In Vivo Micro-Computed Tomography

Prior to micro-CT scanning, mice were anesthetized by intramuscular injection of a mix of Domitor (medetomidine, Orion, Finland; 1 mg/Kg) and Clorketam (ketamine, Vetoquinol, France; 75 mg/Kg). At the end of the scan, animals were given intraperitoneal injection of Antisedan (atipamezolem Orion, Finland; 1 mg/kg). *In vivo* scans were performed using TomoScope ® 30S Duo scanner (CT Imaging, Germany) equipped with two source-detector systems. The operation voltage of both tubes was 40 kV. The integration time of protocols was 90 ms (360 rotations) for 3-cm-long segments and axial images were obtained at an isotropic resolution of 80 μ. Due to the length limit, imaging was performed in 2-4 overlapping parts that were then merged into one dataset representing the entire region of interest. The radiation dose range was 2.1-4.2 Gy.

All micro-CT scans were reconstructed with a filtered back-projection algorithm using scanner software. Then, the reconstructed datasets of each animal were merged using ImageJ software (imagej.net). Three-dimensional volume rendering images were produced using Amira Software (version 5.2.2, Visage Imaging, Inc., Berlin, Germany).

Measurements of Spinal Deformity

To measure the severity of major spinal curves, we calculated the previously described Cobb angle (Cobb, 1948). For that, we first performed *in vivo* CT scan of the entire spine. We then identified the vertebrae that were the most side-tilted rostrally and caudally in the coronal plane, termed end-vertebrae. The angle between a line parallel to the superior end plate of the rostral end vertebrae and a line parallel to the inferior end plate of the caudal end plate was measured. Positive values represent right-sided curves and vice versa.

Morphometric Analysis

To assess the three-dimensional morphology of vertebrae, CT data were analyzed using a predefined index for each plane. We measured the ratios between right and left and between the anterior and posterior vertebral body heights in the coronal and sagittal planes, respectively (Masharawi et al., 2008a). In the axial plane, we identified the center of the posterior lamina of each vertebra and the center of the superior facet joint (Masharawi et al., 2008b). Next, we measured the angle between the center points at each side and calculated the ratio between them.

Image Registration

For qualitative and visual morphological comparison between vertebrae, we matched the surfaces of pairs of vertebrae (control vs *Runx3* mutant or control vs control) by image registration. Because mutant vertebrae exhibited substantial reduction in size we performed isotropic scaling of the target image, resulting in 7 degrees of freedom (DOF; 3 translation, 3 rotation and 1 scale). To that end, we first generated for each image a triangle mesh over the iso-surface corresponding to the external margins of the vertebra, based on an iso-value manually set according to the characteristic density of the imaged vertebra. Then, the orientation and spatial position of each surface was manually standardized, thereby generating an initial approximation of the anatomical match. To fine-tune the match between surfaces, we used the Surface Rigid Registration (srreg) module of the freely available Image Registration Toolkit (IRTK) (Rueckert et al., 1999; Schnabel et al., 2001; Studholme et al., 1999) with a point locator. To allow isotropic scaling during registration, we implemented an iterative algorithm to identify the optimal spatial transformation by multiplying the coordinates of the vertices of the target surface with a scale factor, followed by fine-tuning using the ssreg module. The scale factor was manually set to range from 0.6 to 1, with 0.005 increments. The registration that had reached the minimal score was considered the final transformation.

Gait Analysis

Gait was assessed in 3-month-old mice using the CatWalk XT 10.6 automated gait analysis system (Noldus Information Technology, Wageningen, The Netherlands). Mice were subjected to at least 5 consecutive runs of assessment, each limited by duration range of

2-10 seconds and maximum variation of 20%. Following the identification and labeling of each footprint, gait data was generated. Regularity index (RI), representing the degree of interlimb coordination during gait, is the number of normal step sequence patterns (NSSP) multiplied by the number of paws and divided by the number of paw placements (RI (%) = (NSSP × 4) / no. of placements) (Chen et al., 2014).

Muscle Fiber Area Analysis

We used transverse WGA-stained sections of right or left paravertebral muscles from *Runx3* KO or control mice to include at least 150 individual muscle fibers in each case. ImageJ was used to calculate individual muscle fiber area (μ^2), based on the true scale of the WGA-stained slides.

QUANTIFICATION AND STATISTICAL ANALYSIS

Statistical Analysis

For morphometric analysis, comparisons of quantitative variables between control and mutant mice groups were made by two-sample *t*-test using Bonferroni correction and 95% confidence interval (CI). Calculations were made using R (R Development Core Team, 2016) and ggplot2 (Wickham, 2009). For muscle fiber area analysis, statistical significance of differences in means was determined by a simple Student's *t*-test and defined as $p<0.05$.

Developmental Cell, Volume *42*

Supplemental Information

The Proprioceptive System Masterminds Spinal Alignment: Insight into the Mechanism of Scoliosis

Ronen Blecher, Sharon Krief, Tal Galili, Inbal E. Biton, Tomer Stern, Eran Assaraf, Ditsa Levanon, Elena Appel, Yoram Anekstein, Gabriel Agar, Yoram Groner, and Elazar Zelzer

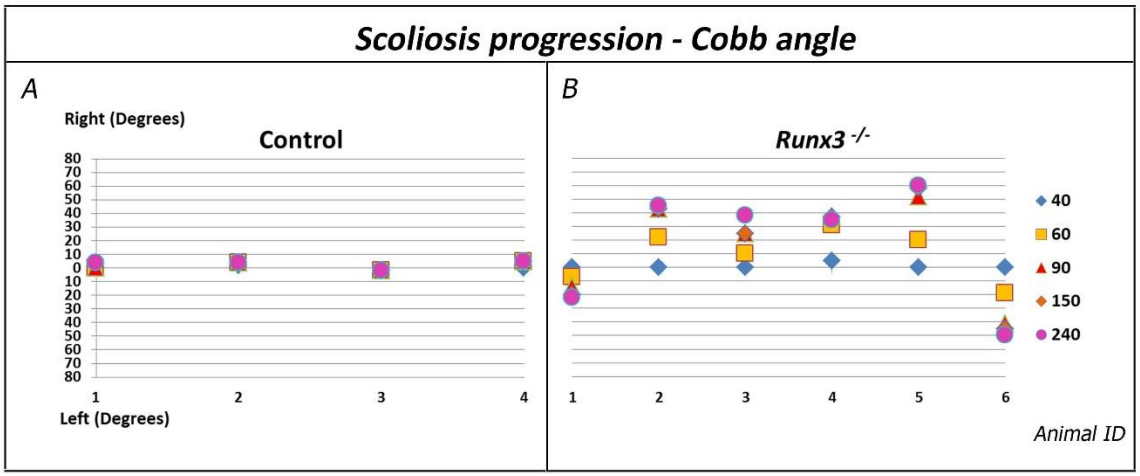

Figure S1. Continued progression of spinal deformity in adult *Runx3* KO mice (related to Figure 1). In vivo CT scans of skeletons of *Runx3* KO mice from P40 throug P240 show that 4 out of 6 mutnts exhibited a mild progression of their spinal deformity after reaching maturity. As expected, spines of control mice remained straight throughout the examined period. The analysis was limited by the higher morbidity and mortality rates of *Runx3* KO mice at these stages relative to the wild type.

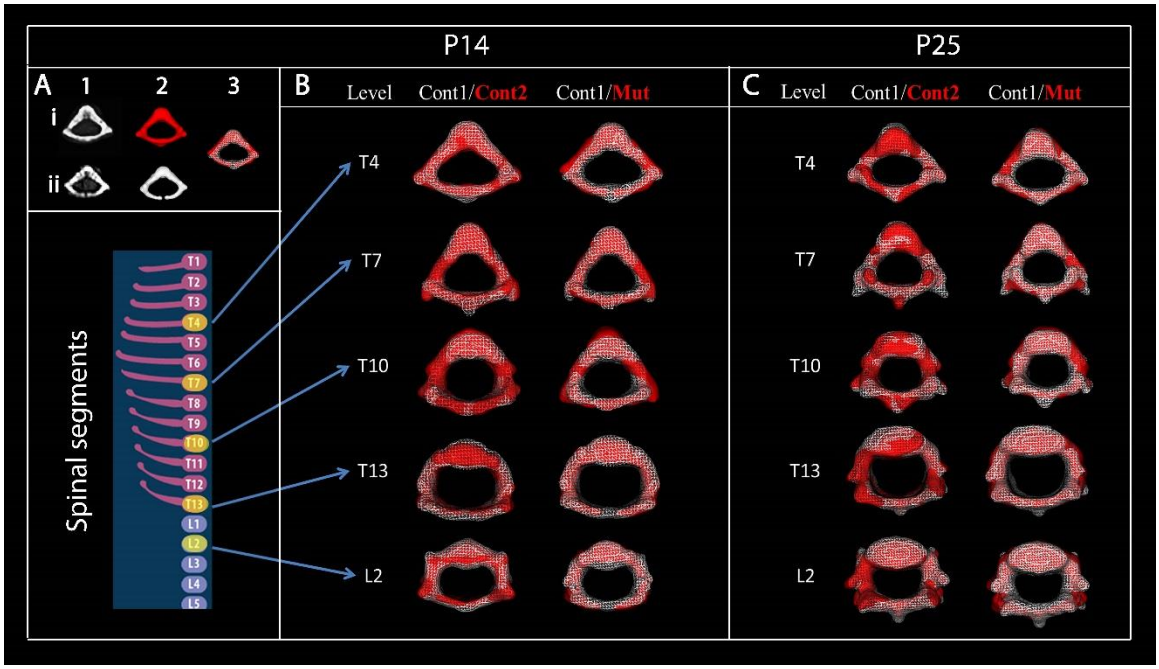

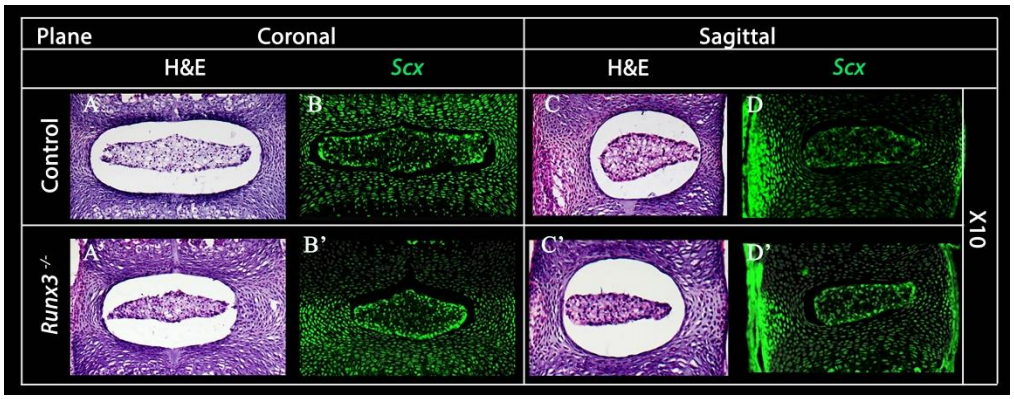

Figure S2. Morphologic comparison of vertebrae and intervertebral discs from wild-type and *Runx3*-deficient mice (related to Figure 2). **(A-C)** Comparison of vertebral morphology. (A): Same-level paired vertebrae from two different animals (i;ii) were CT-scanned (1), reconstructed (2) and registered (3). (B,C): The outer surfaces of paired vertebrae are shown in either white or red. Qualitative morphological assessment by registration in the axial plane revealed at P14 (B) and P25 (C) similar vertebral contours at all examined levels, both between two control mice (Cont1/Cont2) and in mutant vs control (Cont/Mut). (**D-G)** Comparison of D8-D9 intervertebral disc morphology. H&E staining (D,D';F,F') and fluorescent detection of the expression of GFP-coupled scleraxis (E,E';G,G') show similar intervertebral disc morphology in both the sagittal and coronal planes in P3 *Runx3* KO (D'-G') and control mice (D-G).

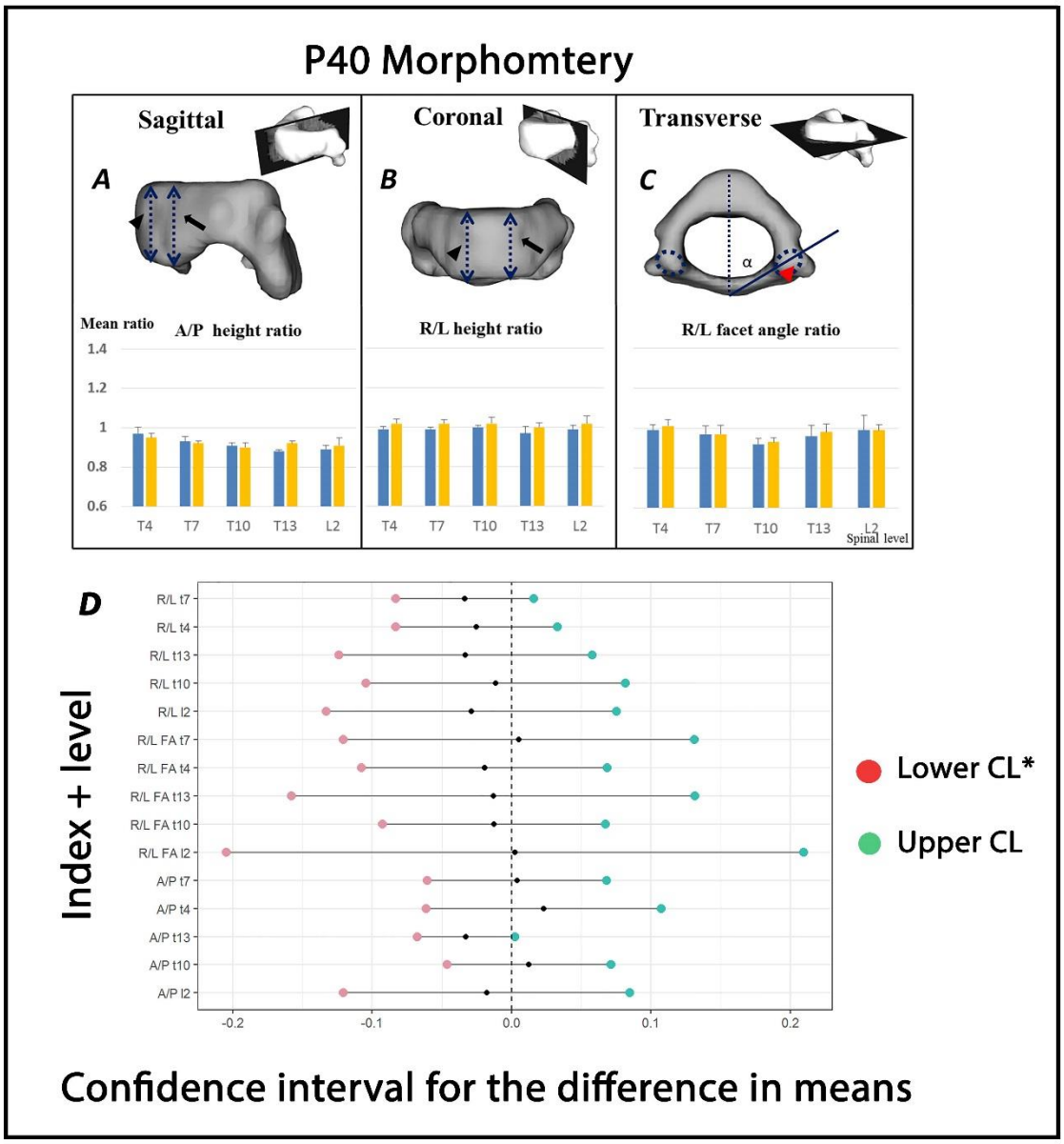

Figure S3. Morphometric analysis of vertebrae at P40 (related to Figure 2). (A-C) Measurements of morphological index ratios that were performed on P25 vertebrae (Fig. 3) was repeated at P40. **(D)** Graph showing the 95% confidence intervals for differences in mean ratios. Similar to the results obtained at P25, the differences in means ratio (represented by black dots) between control and *Runx3* KO mice did not exceed the -0.1-0.1 range in all indices and at all levels (CL, confidence limit).

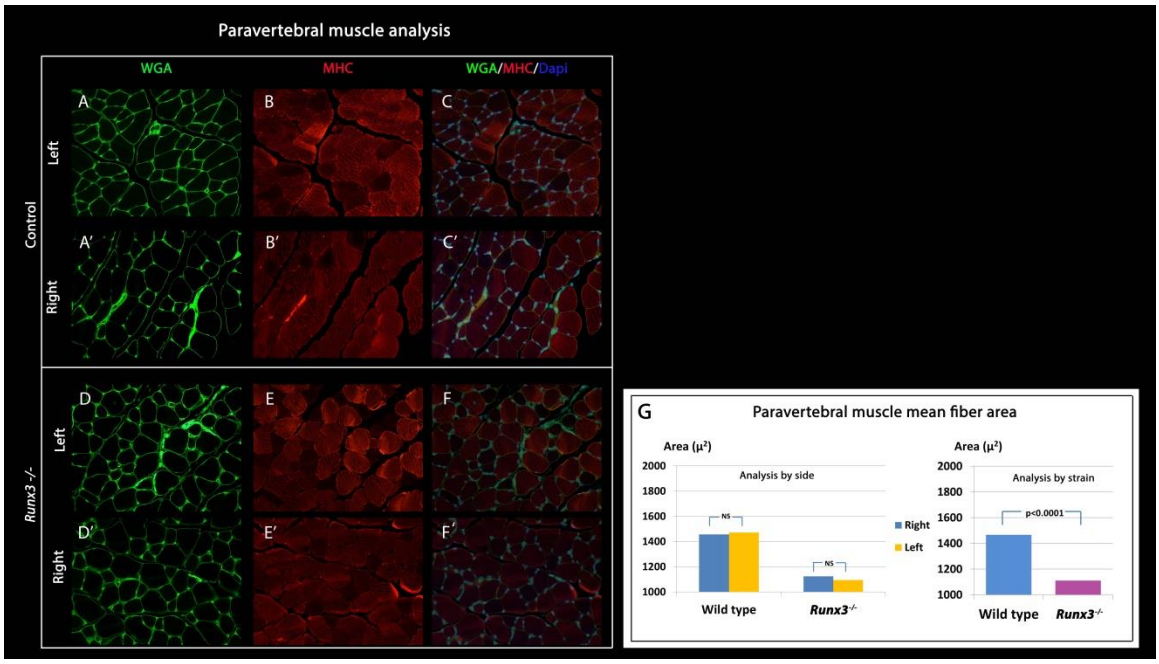

Figure S4. Analysis of paravertebral muscle fibers (related to Figure 2). (A-F) Sections from P30 *Runx3* KO and control paravertebral muscle stained for WGA (A,A',D,D') and myosin heavy chain (MHC) isoform (B,B'; E,E') show similar gross morphology and myosin content of muscle fibers across strains and between right and left sides. C,C',F,F': Merged, DAPI-stained images. **(G)** Graph showing comparisons of mean muscle fiber area between right and left muscles and between *Runx3* KO and control mice. Although no asymmetry was noted in either strain, mean muscle fiber area is significantly reduced in *Runx3* KO animals.

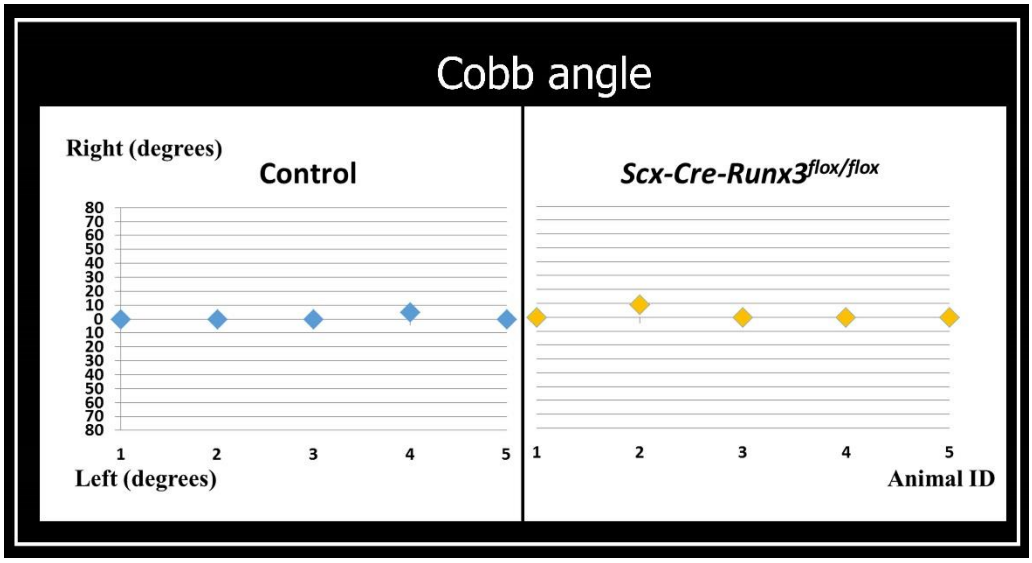

Figure S5. Assessment of spinal deformity in *Scx-Cre-Runx3* cKO mice (related to Figure 3). Graphs show Cobb angle measurements for the cKO strain (left) and control mice (right; *n*=5 in each group), indicating no scoliosis.

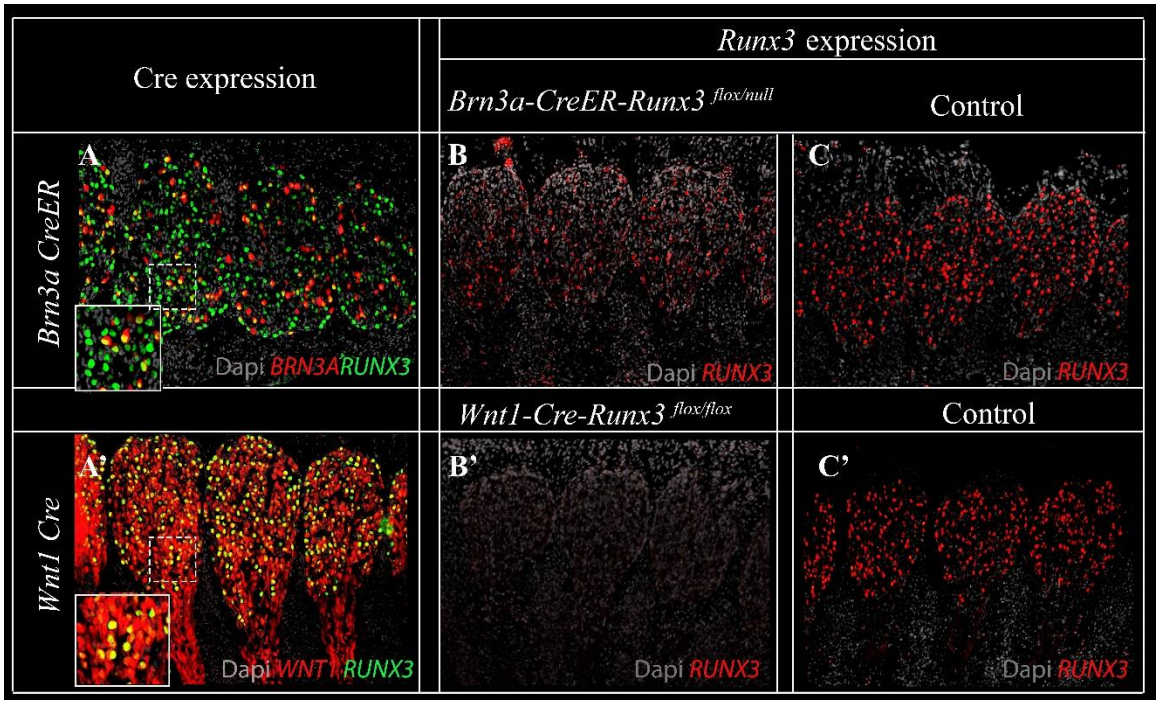

Figure S6. Expression of neural Cre drivers in the DRG and efficiency of *Runx3* deletion in the neural cKO strains (related to Figures 4 and 5). (A,A') Immunostaining for RUNX3 was performed in the DRG of E12.5 *Brn3a-CreER*^{T2} (A) or *Wnt1-Cre* (A') embryos crossed with tdTomato reporter. As indicated by tdTomato detection (red), *Brn3a* is expressed by a subset of cells populating the DRG, whereas *Wnt1* is strongly expressed throughout the region. The higher co-localization (yellow) of *Wnt1* (red) and *Runx3* (green) expression predicts more effective *Runx3* deletion from the DRG in *Wnt1* mutants. Bottom left: Magnifications of the dashed squares. **(B-C')** Whereas in *Brn3a-Cre* driven cKO mice (B, *Brn3a-CreER*^{T2}*-Runx3*$^{flox/null}$) *Runx3* is substantially but partially decreased relative to the control (C), no *Runx3* expression is evident in *Wtn1-Cre-Runx3* cKO mice (B').

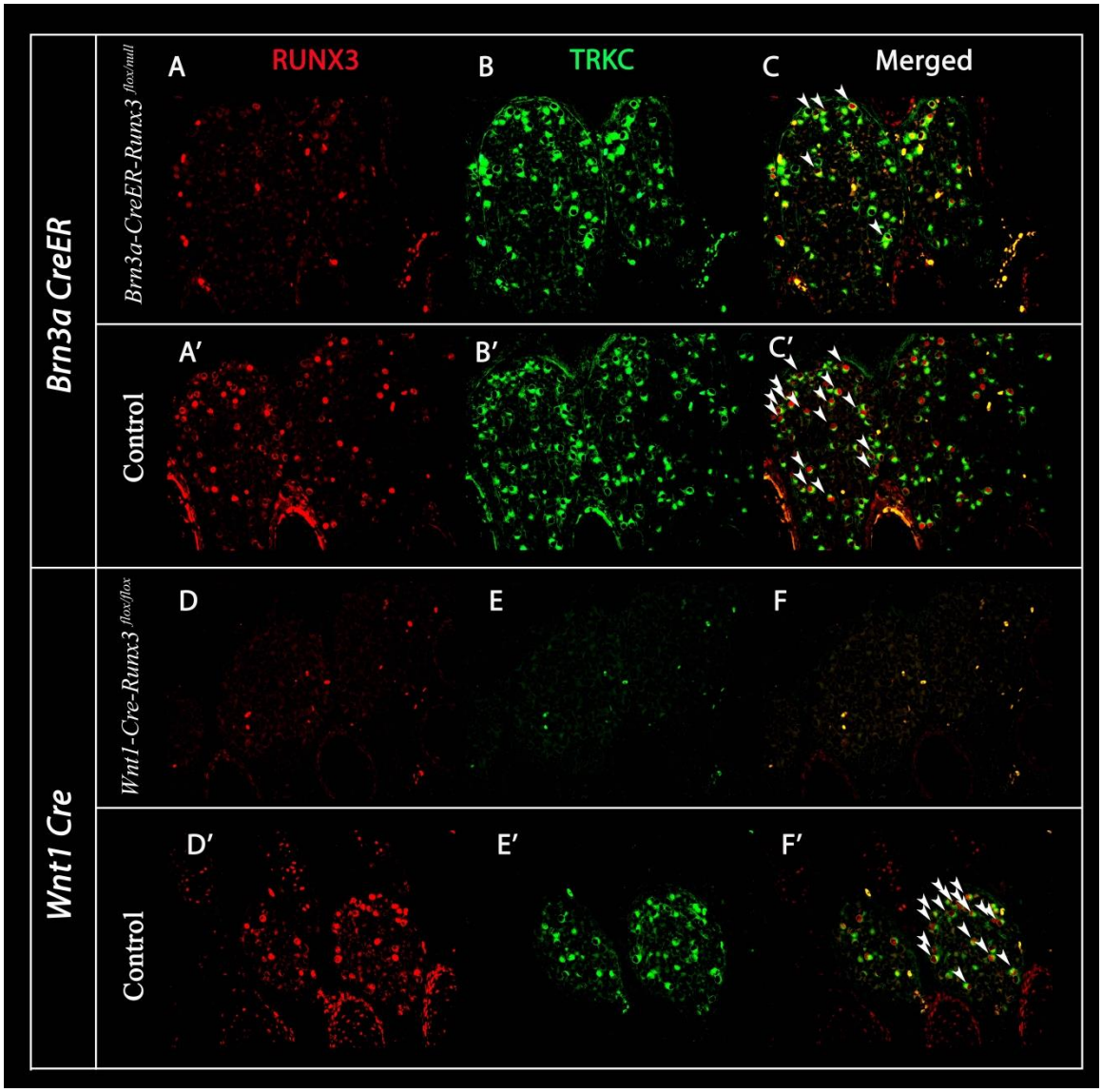

Figure S7. The effect of neural Cre-mediated *Runx3* ablation on DRG proprioceptive neurons (related to Figures 4 and 5). (A-F') Co-immunostaining for RUNX3 (A,A',D,D') and TrKC (B,B',E,E') in DRG sections from E14.5 *Brn3a-CreER^{T2}-Runx3$^{flox/null}$* or *Wnt1-Cre-Runx3$^{flox/flox}$* and control embryos. RUNX3 protein expression (red) was substantially diminished in the *Brn3a*-driven cKO mutant (A) compared to control (A') and undetectable in *Wnt1*-driven cKO (D). Likewise, whereas a few proprioceptive neurons (RUNX3-TrKC double-positive) were detected in DRG of *Brn3a-Runx3* embryos (C; white arrowheads), *Wnt*-driven cKO resulted in complete absence of these neurons.